Journal of
Materials Chemistry A

ROYAL SOCIETY
OF CHEMISTRY

REVIEW

Check for updates

Cite this: *J. Mater. Chem. A*, 2022, **10**, 12788

A potential link between the structure of iron catalysts and Fenton-like performance: from fundamental understanding to engineering design

Ling Li,†[a] Zhuo Yin,†[b] Min Cheng,[a] Lei Qin,[a] Shiyu Liu,[a] Huan Yi,[a] Mingming Zhang,[a] Yukui Fu,[a] Lu Yang,[a] Chensi Tang,[a] Xuerong Zhou,[a] Fuhang Xu,[a] Guangming Zeng *[a] and Cui Lai *[a]

Received 9th March 2022
Accepted 6th May 2022

DOI: 10.1039/d2ta01860h

rsc.li/materials-a

A heterogeneous Fenton-like process on the basis of Fe catalysts has been widely studied for wastewater treatment, which overcomes the problem of the pH limitation and sludge production in homogeneous Fenton systems. Nevertheless, excessive H_2O_2 is typically required to reach a desirable Fenton-like efficiency of Fe catalysts, challenging their environmentally sustainable application. Hence, numerous research studies have been carried out to improve the utilization efficiency of Fe catalysts for H_2O_2. Among various strategies, structural design is possible to endow Fe catalysts with novel physiochemical properties, such as different coordination environments, more active sites and enhanced charge transfer, which has attracted wide interest with tremendous research progress being made. In this review, we mainly focus on the recent advances in designing "smart" Fe catalysts for efficient Fenton-like reactions through structural design. The influence mechanisms of some structural properties (*i.e.*, exposed facet, defects, catalyst size, and space confinement) on the Fenton-like activity of Fe catalysts are carefully discussed to generalize structure–activity relationships. Afterward, we will briefly summarize the characterization techniques for examining these structural properties, followed by strategies to prepare Fe catalysts with a specific structure. This review intends to offer valuable information for designing and fabricating efficient environmental catalysts for a heterogeneous Fenton-like reaction.

1 Introduction

With the inevitable industrialization and urbanization, environmental pollution has developed into a global challenge damaging the ecosystem and plaguing the survival of life.[1–3] Therefore, environmental remediation has received much attention, and finding environmentally friendly techniques to

Ling Li obtained her B.E. degree from the Huazhong Agricultural University, China, in 2017. She is currently in the second year of her PhD in Hunan University under the supervision of Prof. Guangming Zeng. Her current research interests include the fabrication and application of nanomaterials in environment purification.

Guangming Zeng teaches courses and performs research on Environmental Science and Health at Hunan University since 1988. He has been heading of the School of Environmental Science and Engineering since 1994 at the same University. He is one of 2017 Highly Cited Researchers in the world issued by Clarivate Analytics. His current research interests focus on the synthesis and application of functional nanomaterials in the environment and energy field.

---

[a] College of Environmental Science and Engineering, Key Laboratory of Environmental Biology and Pollution Control (Ministry of Education), Hunan University, Changsha, 410082, P. R. China. E-mail: zgming@hnu.edu.cn; laicui@hnu.edu.cn

[b] Department of Urology, Second Xiangya Hospital, Central South University, Changsha 410011, P. R. China

† These authors contributed equally to this article.

remove contaminants from various media is highly urgent.[4–6] Recently, advanced oxidation processes (AOPs) have been regarded as attractive technologies to destruct toxic and recalcitrant pollutants, on account of the generation of highly reactive species.[7–10] The Fenton process is one of the most representative AOPs, which consists of the production of a hydroxyl radical ($^{\bullet}$OH) *via* the interaction between Fe^{2+} and hydrogen peroxide (H_2O_2) (eqn (1)).[11,12] Regrettably, in spite of its powerful oxidation capacity, homogeneous Fenton process keeps facing several limitations, such as accumulation of Fe-containing sludge, narrow working pH (pH 2.8–3.5), and difficulty in catalyst recycling.[13] To this end, researchers have deflected to develop heterogeneous Fenton-like processes based on solid catalysts. The development of efficacious heterogeneous catalysts is significant for the application of this technology.

Currently, multivalent transition metal (*i.e.*, Fe, Mn, Cu and Co) based catalysts are being extensively employed as H_2O_2 activators, because of their capacity of participating in the electron transfer reaction with H_2O_2 and possible auxiliary functions (such as magnetic separation).[14–16] In particular, Fe catalysts show great potential as heterogeneous Fenton-like catalysts since Fe is the second most abundant metal in nature and almost non-toxic; besides, the important role of Fe in classical homogeneous Fenton processes has been widely studied.[17,18] To date, multifarious Fe catalysts have been successively applied in heterogeneous Fenton-like reactions, such as zero-valent Fe,[19,20] Fe oxides,[21,22] Fe-based sulfides,[23,24] Fe-based layered double hydroxides (LDHs),[25,26] and Fe-based metal–organic frameworks (MOFs),[21,27] which do exhibit good Fenton-like catalytic activity. Nevertheless, a large excess of H_2O_2 (above the stoichiometric amount by 100 fold) is typically required to achieve a desirable Fenton-like performance of Fe catalysts,[28] due to the necessary cycle of Fe^{2+} and Fe3+ for $^{\bullet}$OH generation (eqn (1)), and the regeneration of Fe^{2+} *via* reduction of Fe^{3+} (rate-limiting step) (eqn (2)),[29] resulting in the limitation of practical application.

$$Fe^{2+} + H_2O_2 \rightarrow Fe^{3+} + HO^- + {}^{\bullet}OH,\ k = 40\text{–}80\ M^{-1}\ s^{-1} \quad (1)$$

$$Fe^{3+} + H_2O_2 \rightarrow Fe^{2+} + H^+ + HO_2^{\bullet},\ k = 0.001\text{–}0.01\ M^{-1}\ s^{-1} \quad (2)$$

Cui Lai graduated from the College of Environmental Science and Engineering of Hunan University in 2013 and received her Ph.D. degree in Environmental Science. She joined Professor Guangming Zeng's group at Hunan University after completing her Ph.D. degree. Her main research interests are the development and environmental application of functional nanomaterial.

It is thus required to improve the utilization efficiency of Fe catalysts for H_2O_2 to reduce the consumption of H_2O_2. In general, heterogeneous Fenton-like processes are highly dependent on surface reactions to activate H_2O_2 to generate reactive species.[22,30] Therefore, it can be considered that the surface structure of Fe catalysts (*i.e.*, atom arrangement, coordination environment, electronic structure, *etc.*) has a significant impact on their Fenton-like activity.[12,31,32] For example, it is well known that H_2O_2 (Lewis base) tends to adsorb on unsaturated coordinated Fe atoms (Lewis acid sites) on the catalyst surface with strong affinity,[33,34] and the coordination number of active sites usually has a significant effect on the adsorption process. To be specific, the active sites possessing a low atomic coordination number generally exhibit strong adsorption ability, while a too high undercoordination number of active sites might disfavor the adsorption process owing to the relatively strong stereo-hindrance effect.[31,35,36] In this regard, the different coordination environment of Fe, which is closely related to the particle size and exposed surface,[35,37,38] will correspondingly affect H_2O_2 complexation and adsorption, and thus H_2O_2 activation. Meanwhile, the charge transfer from catalysts to H_2O_2 also plays a significant role in activating H_2O_2, and sufficient charge transfer would effectively promote the catalytic activity of catalysts. Accordingly, many strategies to optimize the electronic structure of Fe catalysts have been proposed, such as introducing oxygen vacancies, which can not only facilitate the surface Fe^{3+}/Fe^{2+} redox cycle, but also promote charge transfer from catalysts to adsorbed H_2O_2, thereby improving H_2O_2 utilization efficiency and Fenton-like catalytic performance.[39–41] As a whole, the structural design of Fe catalysts to modulate the surface structure brings about new opportunities for improving Fenton-like catalytic activity. A systematic understanding of the relationship between Fenton-like catalytic activity/mechanisms and structural characteristics is thus in urgent need for future construction of highly efficient Fe catalysts.

Recently, a number of reviews have summarized the types of Fe catalysts in heterogeneous Fenton-like processes and strategies to improve catalytic performance through additional energy input, such as light, ultrasound, and chelating agents.[12,17,31,42–44] These reviews made great progress in summarizing and promoting the application of heterogeneous Fenton-like processes based on Fe catalysts. However, to the best of our knowledge, there is no review focused on the structural design of Fe catalysts towards enhanced Fenton-like processes. In this critical review, we begin with the specific influence of the structural properties of Fe catalysts including the exposed surface, defects, catalyst size, and space confinement on Fenton-like activity, which have typical impacts on the atomic and electronic structures of catalysts, and then, advanced characterization techniques for evaluating the structure–performance relationship are introduced. Besides, structural engineering strategies are also discussed in detail. It is hoped that the available and up-to-date information in this review will inspire researchers to further design heterogeneous catalysts with respect to structural design to maximize their potential for environmental remediation.

2 Key features of the structure

In order to take full advantage of structural design of Fe catalysts for Fenton-like catalysis, it is necessary to better understand the influence mechanism of structural properties on the Fenton-like catalytic performance. In this section, we emphasize some key features of the structure, including the exposed surface, defects, catalyst size, and space confinement, which significantly affect the surface structures of Fe catalysts and thus Fenton-like performances.

2.1 Exposed surface

To date, numerous studies have demonstrated that rationally modulating the exposed surface of Fe catalysts is an available strategy to enhance their Fenton-like catalytic activity, because the distinguishing surface atomic configuration and coordination on different surfaces usually have a notable impact on the surface reactivity.[35,45–47] Here, the substantial role of the Fe catalyst surface in affecting Fenton-like reactions will be demonstrated from the perspective of H_2O_2 adsorption, surface electronic structures relating to H_2O_2 activation, and $^{\bullet}OH$ transformation.

Generally, the effective adsorption of H_2O_2 on the Fe catalyst surface is considered as a prerequisite for the subsequent H_2O_2 activation process. In a typical process, H_2O_2 can be molecularly adsorbed onto catalysts *via* the interaction between the hydroxyl groups of H_2O_2 and those on the catalyst surface, the interaction between the O atoms of H_2O_2 and surface exposed metal atoms, or other surface processes.[48,49] The adsorption behaviors are closely related to the atomic arrangement over the catalyst surface. Therefore, it can be inferred that the exposed surface with different atomic arrangements is possible to influence the chemisorption state of H_2O_2 on the surface and then affect the catalytic process.[50–52] For example, Dai *et al.* reported that the $CuFeO_2$ (110) surface exposed more Fe and Cu atoms than the $CuFeO_2$ (012) surface, while the exposure of O, Fe, and Cu atoms was more uniform on the (012) surface. Consequently, the chemisorption state of H_2O_2 on these two surfaces was different, and a favorable configuration between H_2O_2 and the (012) surface was formed with an O–H–O bond (1.749 Å) smaller than that on the (110) surface (2.472 Å), and the O–O bond within H_2O_2 being suitably elongated (from 1.468 Å to 1.472 Å), which favored electron transfer and $^{\bullet}OH$ generation (Fig. 1(A–D)).[53] Likewise, H_2O_2 could be adsorbed onto Fe–Co Prussian blue analogue (100) and (111) surfaces with different chemisorption states and adsorption energy, which subsequently had an effect on the generation of $^{\bullet}OH$.[52]

In addition, according to previous research, the different atomic arrangements and coordination on each surface will also lead to anisotropic surface electronic structures and thus surface charge states,[38,54,55] which may correspondingly result in

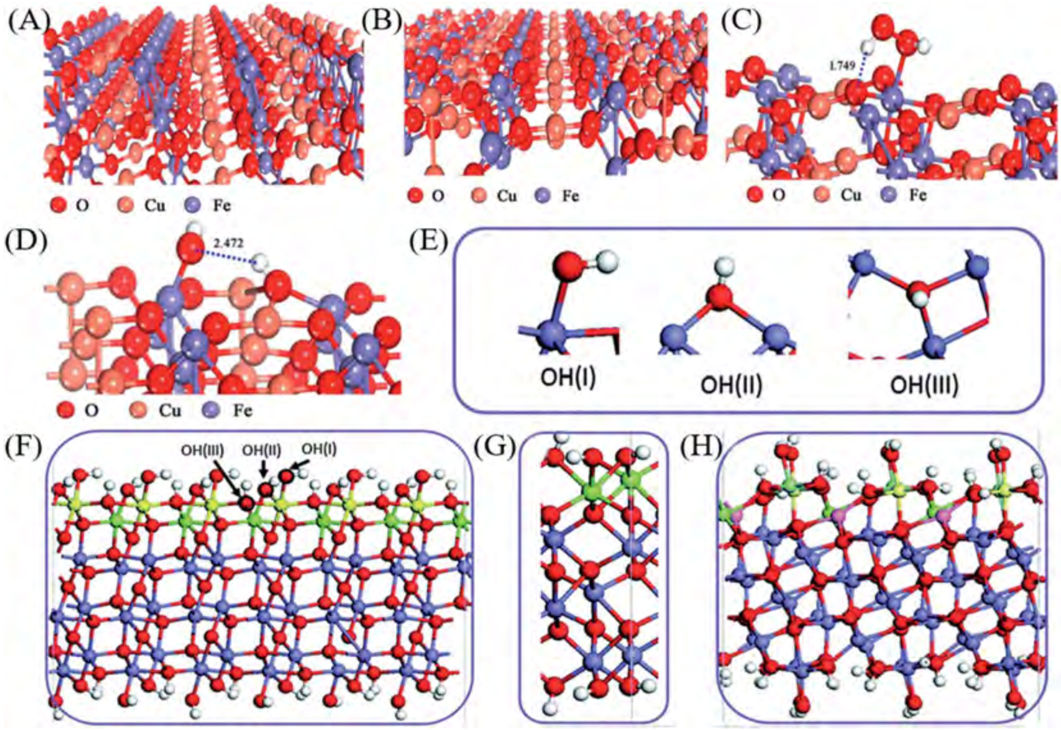

Fig. 1 Optimized surface structures of (A) $CuFeO_2$ (012) and (B) $CuFeO_2$ (110); (C) H_2O_2 adsorption on $CuFeO_2$ (012) and (D) H_2O_2 adsorption on $CuFeO_2$ (110). Reprinted with permission from ref. 53, Copyright 2018, American Chemical Society; (E) schematic drawing of singly, doubly and triply terminating OH groups, where O is in red, H is in white and the other color represents Fe atoms; (F) side views of optimized α-Fe_2O_3 (104) surfaces, where top-layer Fe atoms are in two groups highlighted in yellow and green colors; (G) side views of optimized α-Fe_2O_3 (001) surfaces, where top-layer Fe atoms are in green; and (H) side views of optimized α-Fe_2O_3 (113) surfaces, where top-layer Fe atoms are in four groups highlighted in yellow, blue, pink and green, respectively. Reprinted with permission from ref. 38, Copyright 2015, Royal Society of Chemistry.

the variation of charge transfer from catalysts to H_2O_2. As revealed by Chan *et al.*, there were three types of OH groups including singly coordinated OH groups ($OH_{(I)}$), doubly coordinated OH groups ($OH_{(II)}$), and triply coordinated OH groups ($OH_{(III)}$) on the hematite surface. As seen from Fig. 1(E–H), Fe atoms would coordinate with different types and numbers of OH groups at each exposed surface. Consequently, Fe atoms on α-Fe_2O_3 (001), (104), and (113) surfaces exhibited different oxidation states due to the distinguishing coordination environment. To be specific, Fe cations on the (001) surface mainly existed in the valence state of 3+, and primarily showed an oxidation state between 2+ and 3+ on (113) and (104) surfaces. The hematite (113) and (104) surfaces thus more easily initiated an electron transfer to activate H_2O_2.[38] Besides, Huang *et al.* drew a conclusion that surface-reactivity differences appeared to be more relevant with the extent of undercoordination of Fe sites rather than their simple aerial density. They found that the hematite (012) surface possessed higher densities of undercoordinated Fe sites (singly undercoordinated Fe action activate sites (Fe_{1uc})) than the hematite (001) surface (3-fold undercoordinated Fe action active sites (Fe_{3uc})), while the hematite (001) surface showed higher photo-Fenton catalytic activity. This might be because more highly undercoordinated surface Fe^{3+} was more readily reduced to Fe^{2+}, thus promoting H_2O_2 activation and $^{\bullet}OH$ generation.[30]

Furthermore, when H_2O_2 is dissociated to $^{\bullet}OH$ at the catalyst surface, the generated $^{\bullet}OH$ may either bound to the surface ($^{\bullet}OH_{surface}$) or diffused to the solution ($^{\bullet}OH_{free}$).[56–58] This is thought to be related to the catalyst surface structure because the different atom arrangement may affect the binding of $^{\bullet}OH$ to the catalyst surface. For instance, Li *et al.* revealed that high-density oxygen atoms on the BiOCl (001) surface tended to impede the binding of $^{\bullet}OH$ to the surface owing to their steric hindrance, while the Bi_{3c} sites on the BiOCl (010) surface could provide Lewis-acid sites for the stabilization of $^{\bullet}OH$. Therefore, $^{\bullet}OH_{free}$ was primarily generated when employing BiOCl (001) as a Fenton-like catalyst, and $^{\bullet}OH_{surface}$ was dominant in the BiOCl (010)/H_2O_2 system.[57] By this way, the non-selective $^{\bullet}OH$ is possible to selectively degrade organic pollutants during Fenton-like reactions since $^{\bullet}OH_{surface}$ prefers to react with organic pollutants showing high affinity to the catalyst surface, and organic pollutants with low affinity to the catalyst surface could be easily oxidized by $^{\bullet}OH_{free}$. However, the relevant studies on Fe catalyst-based Fenton-like reactions are rare, which need more research focus in the future.

Overall, the exposed surface of Fe catalysts is an important factor that affects Fenton-like performance owing to the close ties between surface properties and H_2O_2 activation. Nevertheless, it should be noted that single crystal facets of metallic Fe do not have any application potential. Meanwhile, theoretical simulations based on density functional theory (DFT) calculation provide available information to understand the Fenton-like catalytic mechanism on different exposed surfaces by modeling the interfacial adsorbate–adsorbent interactions. Meanwhile during the optimization process, the water molecule and other possible co-existing ions such as Cl^- and Na^+ in solution are generally neglected.[59] In order to make the simulation consistent with the experimental solution environment, self-consistent reaction fields with the solvent model density (SMD) model are suggested to be employed.[60,61]

2.2 Defects

Defect engineering of Fe catalysts has also been proven as an effective strategy to fine-tune the Fenton-like catalytic performance since the existence of defects can usually modify the surface electronic structure, improve the charge transfer, or act as the active sites for H_2O_2 activation.[11,39] Generally speaking, defects in Fe catalysts can be classified into two major categories, that is, dopants and vacancies.[12]

For elemental doping, the doped atoms may substitute the position of original atoms or enter into the interstitial void, and most probably, act as active sites for H_2O_2 activation or result in the variation of electron distribution owing to the different properties such as electronegativity between doped atoms and original atoms.[62–64] Taking S-doped $CoFe_2O_4$ as an example, it can be found that the charge density of the Fe–S bond and Co–S bond increased after S-doping (Fig. 2(A and B)), and this would facilitate the redox cycle between surface Fe^{3+}/Fe^{2+} and Co^{3+}/Co^{2+}, leading to the existence of more Fe^{2+} and Co^{2+}. In this regard, sufficient $^{\bullet}OH$ could be generated with adding a small amount of H_2O_2 and contributed to efficient pollutant degradation.[65] Likewise, Panjwani *et al.* revealed that the higher electronegativity of Fe in comparison with Mn led to electron transfer from Mn atoms to Fe atoms through the Fe–O–Mn bond, and then an electron-poor center was formed around Mn and an electron-rich center was formed around Fe in Fe–Mn–SiO_2. This unique electron structure thus facilitated H_2O_2 activation and reactive species generation.[66] Meanwhile, the nonuniform distribution of surface electrons caused by doping metal ions with lower oxidation states may also result in the generation of oxygen vacancies, ascribed to charge compensation effects.[67,68] For example, Soltani *et al.* reported that the oxygen vacancy concentration increased when increasing the doping amount of Ba in $Bi_{1-x}Ba_xFeO_3$, and the mechanism was related to the neutralization of charges produced by lower-valence Ba^{2+} substituting Bi^{3+}.[69]

In fact, oxygen vacancies as another crucial defect in Fe catalysts have also attracted an explosion of research interest in Fenton-like catalysis. As is well known, oxygen vacancies are the most common anion vacancies in Fe oxide or Fe-based LDHs, and most recent studies have demonstrated the positive role of oxygen vacancies in promoting Fenton-like catalytic activity.[11,41,70,71] On the one hand, it is reported that the oxygen vacancies with abundant localized electrons and coordinative unsaturated nature can significantly promote the adsorption of H_2O_2 molecules.[72,73] Meanwhile, the interaction of oxygen vacancies with H_2O_2 usually results in the suitable elongation of the O–O bond, thereby benefitting the subsequent H_2O_2 activation process.[40,41] Taking hollow sphere $CuFe_2O_4$ containing oxygen vacancies (HS $CuFe_2O_{4\text{-}\sigma}$) as an example, H_2O_2 would be absorbed onto $Fe^{III}_{0.5}Cu^{II}_{0.5}$ sites on the $CuFe_2O_4$ surface and oxygen vacancy sites on the HS $CuFe_2O_{4-\sigma}$ surface with an adsorption energy of −0.558 eV and −5.982 eV and an O–O

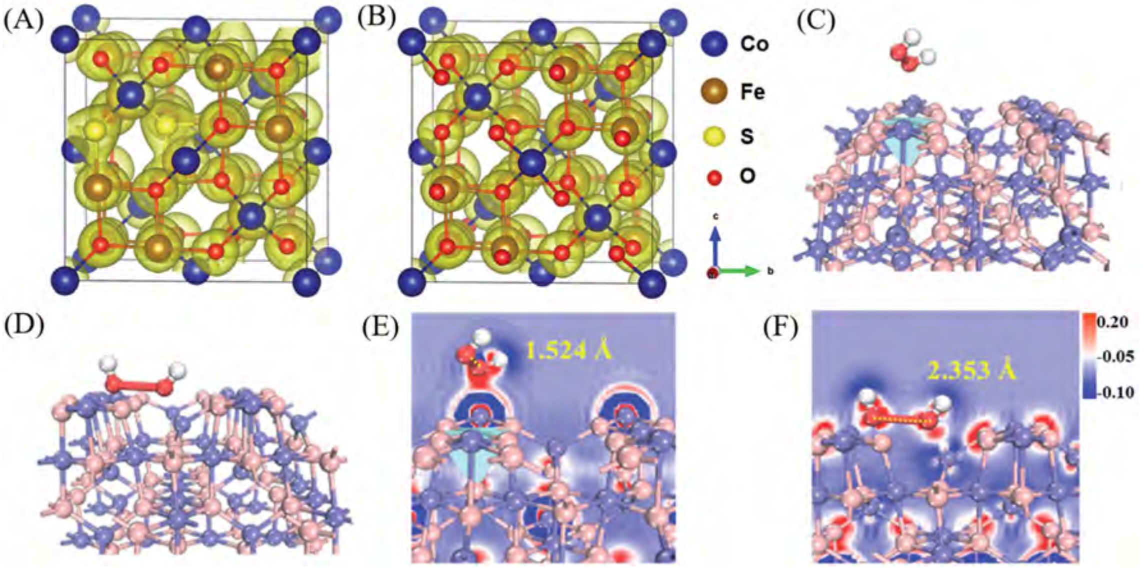

Fig. 2 Charge density diagrams of (A) S–$CoFe_2O_4$ and (B) $CoFe_2O_4$; reprinted with permission from ref. 65, Copyright 2021, Elsevier; optimized geometry of the absorption structure of H_2O_2 on (C) the $CuFe_2O_4$ (110) $Fe^{III}_{0.5}Cu^{II}_{0.5}$ site and (D) the $CuFe_2O_{4-\sigma}$ (110) oxygen vacancy site; charge density of H_2O_2 on (E) the $CuFe_2O_4$ (110) $Fe^{III}_{0.5}Cu^{II}_{0.5}$ site and (F) the $CuFe_2O_{4-\sigma}$ (110) oxygen vacancy site. The purple spheres at the tetrahedral position and octahedral position denote the composition of Fe and $Fe_{0.5}Cu_{0.5}$, respectively, and the red and white spheres represent O and H atoms, respectively. Reprinted with permission from ref. 11, Copyright 2021, Elsevier.

bond length of 1.524 Å and 2.353 Å, respectively (Fig. 2(C–F)). As a result, HS $CuFe_2O_{4-\sigma}$ exhibited better Fenton-like activity than $CuFe_2O_4$.[11] On the other hand, the localized electrons adjacent to oxygen vacancies are more likely to migrate, which can accelerate the surface Fe^{3+}/Fe^{2+} redox cycle and promote H_2O_2 activation to generate $^{\bullet}OH$.[12,74] More importantly, previous studies have shown that the existence of oxygen vacancies possibly reduces the coordination number of nearby metal sites.[75,76] For instance, Wang *et al.* revealed that the Fe–O coordination number (3.4) in 2D Fe_3O_4 containing ample oxygen vacancies was lower than that in commercial Fe_3O_4 (4.6).[77] This will correspondingly affect Fenton-like catalytic performance since the coordination number of surface Fe sites is closely related to the H_2O_2 adsorption and activation process.[30,51] Except for oxygen vacancies, the promoting effects of some other anion vacancies (*i.e.*, sulfur vacancies in Fe sulfide) on Fenton-like processes have also been reported with a similar mechanism to oxygen vacancies.[78–80]

From the above all, it can be reckoned that the presence of defects possibly promotes Fenton-like reactions through creating a strong synergistic effect. Nevertheless, it should be emphasized that excessive defects may result in the deterioration of structural stability and electrical conductivity, and even lead to structural collapse.[67] Therefore, it is significant to introduce an appropriate number of defects to regulate the surface structures such as surface atom coordination and electron distribution of Fe catalysts for improved Fenton-like performance.

2.3 Catalyst size

The size of Fe catalysts is also considered as a crucial factor for determining H_2O_2 activation performance and reactive species generation, which can be explained by the clear correlation between the catalyst size and utilization efficiency of active sites.[37,81] To be specific, larger catalyst particles may possess uneven aggregation of hundreds or thousands of metal atoms, and only a small fraction of them on the surface are exposed to reactants. When decreasing the particle size, the fraction of active atoms (on the surface) in the total number of atoms can be significantly increased due to fewer atoms aggregating together.[36,37,82,83] The exposure of active sites to reactants could thus be increased, leading to higher active site utilization efficiency. In this regard, compared to Fe catalysts with sizes of nanoparticles and nanoclusters, single Fe atoms can achieve the highest utilization of metal active sites and then attain ultrahigh activities.[84] Nevertheless, single metal atoms have high surface free energy, which are likely to aggregate during the preparation process. Therefore, appropriate supports such as carbon substrates, $g\text{-}C_3N_4$, and metal oxides are typically required to stabilize single metal atoms by forming strong bonds.[82,85,86] For example, Yin *et al.* found that confined space and Si-OH groups of SBA-15 contributed to the successful formation of single Fe atom sites, where Fe atoms could substitute H atoms of Si-OH to form an Fe–O bond for stabilization. Benefitting from the maximized atomic utilization, SAFe-SBA exhibited a much higher Fenton-like degradation rate of phenol (100% in 90 min) than SBA-15 loaded $\alpha\text{-}Fe_2O_3$ (80.3% in 180 min).[87]

Except for the highest utilization of metal active sites, the unsaturated coordination environment and unique electronic structure of reactive sites in single atom catalysts (SACs) also benefit the improvement of catalytic activity.[81,82,88] For instance, some studies proposed that N atoms in the support materials could mightily anchor individual metal atoms to form a metal–

N coordination, and the strong interaction of metal sites with neighboring pyridinic-N or pyrrolic-N then influenced the electron density of single-atom metal sites, thereby affecting the charge transfer between the metal and H_2O_2 molecule.[89,90] As shown in Fig. 3(A and B), Su *et al.* found that an atomic Fe–N_4 center was achieved in both carbon nitride loaded single Fe atoms (Fe_1/CN) and carbon nitride with abundant nitrogen vacancy loaded single Fe atoms (Fe_1-N_v/CN), and the adsorption edge position of Fe_1-N_v/CN was lower than that of Fe_1/CN, indicating a higher electron density of Fe sites in Fe_1-N_v/CN, which promoted H_2O_2 activation to generate $^{\bullet}$OH.[91] In another case, single Fe atoms could be anchored onto three-dimensional N-doped carbon nanosheets (Fe/NC) by forming an Fe–N–C bond. During a catalytic reaction, N atoms could attack electrons from the adjacent C atoms and transfer to the Fe atoms coordinated with them. This specific electronic configuration and electron-transfer process then led to the outstanding catalytic activity of Fe/NC.[92]

Nevertheless, the long-term stability of single atom catalysts come into question because the interaction between reactants and single atoms may weaken the interaction between the support substrate and single atoms and therefore result in the migration and aggregation of single atoms during the reaction process if single atoms bound weakly to the support.[90,93] Taking the Pt atoms on the Fe_3O_4 (001) surface as an example, Bliem *et al.* found that Pt atoms agglomerated into sub-nanometer Pt clusters after adsorption of CO, since the formation of Pt(CO) species weakened the atom–support interaction and increased the mobility of Pt atoms.[94] Recently, some suitable and effective methods such as enhancing the metal–support interactions or confining the single metal atoms in limited space have been proposed to improve the stability of SACs during the reaction.[37,95,96] Zuo *et al.* synthesized a sandwich structure stabilized atomic Fe catalyst by anchoring single Fe atoms into a g-C_3N_4–rGO support possessing a double-layered structure. The stability of g-C_3N_4–Fe–rGO increased in comparison with g-C_3N_4–Fe, which could be ascribed to the fact that the double layer confined structure and extra Fe–O bond between Fe and rGO could further stabilize the atomically dispersed Fe sites.[97] Besides, it was also proposed that the strongly coordinated N–M bond produced from pyrolyzing MOFs endowed SACs with increased stability.[93,98] According to the above discussion, the development of an atomic Fe catalyst brings about new insights for enhancing Fenton-like catalytic activity. However, the application of single Fe atoms in Fenton-like processes is still in infancy, and it is significant to investigate the reaction process optimization and the structure–catalysis relationships in future studies.

2.4 Nanoconfinement

Nanoconfinement generally refers to the nanosized special restriction provided by catalysts.[99] As a novel nanotool, it has been employed in Fe-based heterogeneous Fenton-like systems to minimize the mass transfer limitation. Some studies have proposed that under a nanoconfined environment, the space where the reaction occurs is restricted, that is, the distance

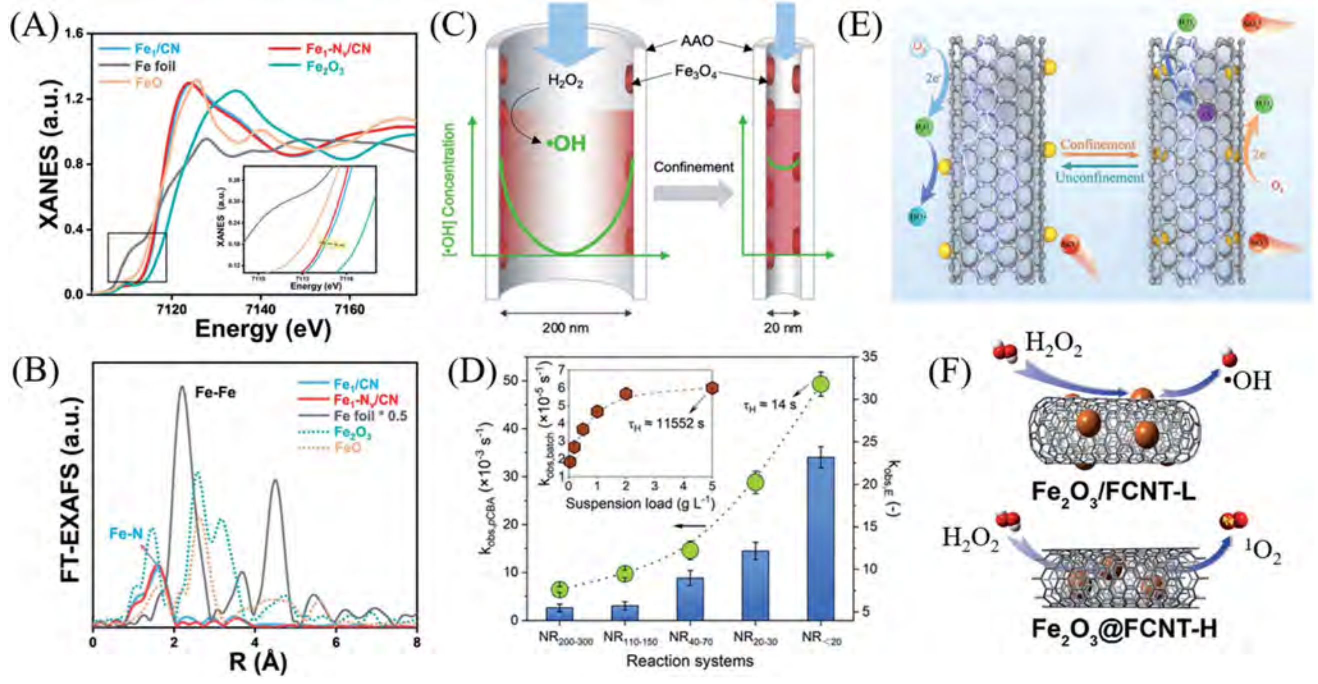

Fig. 3 (A) Fe K-edge XANES spectra of Fe_1/CN, Fe_1-N_v/CN, standard Fe foil, FeO, and Fe_2O_3, and (B) Fourier-transformed (FT)-EXAFS curves in *R* space. Reprinted with permission from ref. 91, Copyright 2021, Wiley; (C) the diffusion of $^{\bullet}$OH in Fe_3O_4-AAO with different pore sizes, and (D) pseudo-first-order rate constants in the nanoreactor series (left *y*-axis). Reprinted with permission from ref. 105, Copyright 2020, American Chemical Society; (E) possible reaction mechanism in the Fe_2O_3-in-CNT/H_2O_2 system and Fe_2O_3-out-CNT/H_2O_2 system. Reprinted with permission from ref. 109, Copyright 2021, American Chemical Society; (F) illustration of the possible mechanism in the Fe_2O_3@FCNT-L/H_2O_2 system and Fe_2O_3@FCNT-H/H_2O_2 system. Reprinted with permission from ref. 110, Copyright 2019, PNAS.

between the "catalyst surface" and "reactants" will be controlled to a certain length scale. Then, the as-generated reactive species in close vicinity to target organic pollutants have more chances to attack these molecules, thereby benefiting the usage of the reactive species.[100–102] According to a literature survey, the availability of reactive species, of which the concentration is strongly related to the diffusion distance can be greatly affected when varying the length scale of nanoconfinement.[103–105] Taking the degradation of *para*-chlorobenzoic acid with an Fe_3O_4-anodized aluminum oxide (AAO) nanoreactor as an example (Fig. 3(C and D)), the diffusion of $^{\bullet}OH$ could be significantly minimized at a nanoconfined pore size below 25 nm. Consequently, nanoreactors with a smaller pore size achieved much higher degradation kinetics (*i.e.*, 4.93×10^{-2} s^{-1} for nanoreactors$_{<20}$) than those with a larger pore size (*i.e.*, 6.4×10^{-3} s^{-1} for nanoreactors$_{200-300}$).[105]

In addition to reactive species utilization, controlling the length scale of nanoconfinement also provides an opportunity for the interception of macromolecules and traverse of small molecules, thus achieving the selective degradation of target organic pollutants.[101,106] During this process, the key factor is the quite different size between the coexisting multicomponent organic pollutant and target organic pollutant. Furthermore, some other studies also proposed that confining Fe catalysts into carbon nanotubes (CNTs) might provide novel insight into the Fenton-like catalytic mechanism, because the curvature of CNT walls may give rise to the shift of the π electron of graphene layers from the inner to the outer surface and leads to a potential difference, and therefore the nanoparticles confined inside CNTs will exhibit different properties and chemical activities from those on the outer surface of CNTs.[107,108] For example, Guo *et al.* found that an Fe_2O_3-out-CNT/H_2O_2 system without nanoconfinement would activate H_2O_2 to generate $^{\bullet}OH$, while $^1O_2$ was considered as the dominant reactive species in an Fe_2O_3-in-CNT/H_2O_2 system under nanoconfinement, which might be explained by the interaction of generated $HO_2^{\bullet}/^{\bullet}O_2^-$ with H_2O_2 or $^{\bullet}OH$ within confined space (Fig. 3(E)).[109] A similar result was reported by Yang *et al.* using CNTs for nanoconfinement (Fig. 3(F)).[110] All these research results provide useful guidance for employing nanoconfinement to enhance the Fenton-like performance of Fe catalysts.

3 Characterization technologies to determine structural properties

After understanding the impacts of structural properties on the Fenton-like catalytic performance, it is essential to introduce the characterization technologies which can evaluate the achievements of structural design. The obtained information is helpful for understanding the structure–activity relationship and providing a basic guide for rational structural design. Therefore, in this section, we will summarize some common characterization techniques for examining the above structural properties (Table 1).

3.1 Characterization techniques for the exposed surface

Typically, transmission electron microscopy (TEM) characterization can be used to identify the exposed surface of materials based on information about lattice parameters.[46,127] Taking Fe_3O_4 nanoparticles as an example, a lattice spacing of 0.486 nm could be observed in the high-resolution TEM (HR-TEM) image of Fe_3O_4 nano-octahedrons (Fig. 4(A)), which was close to the (111) planes of Fe_3O_4. Meanwhile, the corresponding Fast Fourier Transform (FFT) image was closely related to the diffraction from the crystal planes of Fe_3O_4, and all of this

Table 1 Summary of characterization technologies to determine structural properties

Characterization techniques	Structural properties	Detailed information	References
SEM/TEM	Catalyst size (nanoparticles and nanoclusters), nanoconfinement	Morphology in the nanoscale range	46, 55 and 111
HR-TEM	Exposed surface	Lattice parameters	55 and 112
HAADF-STEM	Catalyst size (single atom), nanoconfinement	Morphology in the sub-angstrom range, visual confirmation of atom distribution	97, 109 and 113
STM	Catalyst size (single atom)	Atomic sites and corresponding electronic structures	114–116
EDX-mapping	Defects	Surface element composition	117 and 118
XRD	Exposed surface	Crystal structure, peak intensity	38 and 119
XPS	Defects, nanoconfinement	Surface elements composition, chemical state of elements near the surface	11, 110 and 120
XAS	Defects, catalyst size (single atom)	The local bonding environments, (*i.e.*, coordination number and interatomic distance), chemical states of specified elements	121–123
EPR	Defects	Fingerprinting information about the unpaired electrons	71 and 124
N_2 adsorption–desorption isotherms	Nanoconfinement	Brunner–Emmet–Teller (BET) surface area and pore volume	125 and 126

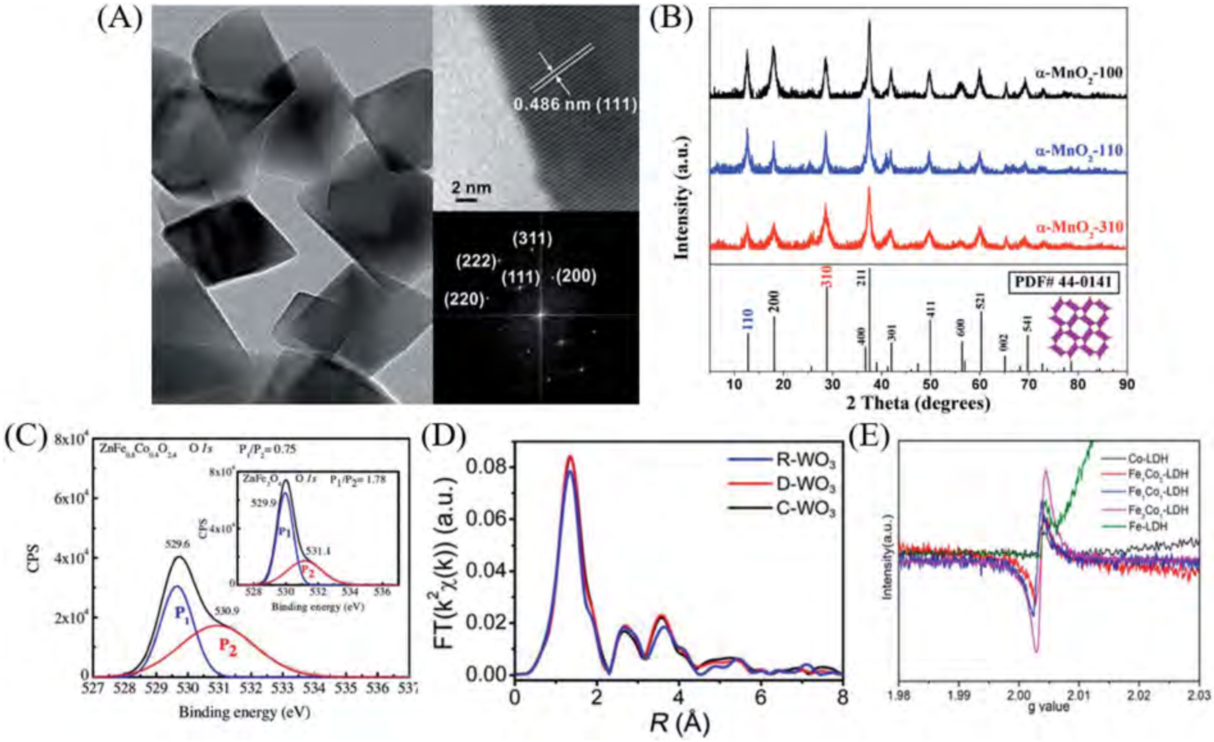

Fig. 4 (A) TEM, HRTEM images (upper right insets), and Fourier transform images (lower right insets) of Fe_3O_4 nano-octahedrons. Reprinted with permission from ref. 55, Copyright 2017, American Chemical Society; (B) XRD patterns of α-MnO_2 with different exposed facets. Reprinted with permission from ref. 119, Copyright 2018, American Chemical Society; (C) O 1s XPS spectra of $ZnFe_{0.8}Co_{0.4}O_{2.4}$ (the insert shows the O 1s XPS spectra of $ZnFe_2O_4$). Reprinted with permission from ref. 120, Copyright 2020, Elsevier; (D) Fourier-transform W L_3-edge EXAFS spectra of the samples in reference to commercial WO_3. Reprinted with permission from ref. 135, Copyright 2016, American Chemical Society; (E) EPR spectra of the synthesized LDHs. Reprinted with permission from ref. 71, Copyright 2020, Elsevier.

information suggested that Fe_3O_4 nano-octahedrons were mainly enclosed by (111) planes.[55] In another case, the HR-TEM image and corresponding FFT pattern confirmed that $FeWO_4$-010 nanosheets and $FeWO_4$-001 nanosheets were predominantly exposed with a (010) surface and (001) surface, respectively.[112]

Apart from HR-TEM, X-ray diffraction (XRD) can also provide useful information to confirm the major exposed surface of materials. In general, XRD is an analytical tool for investigating the crystalline structure, each diffraction peak in the XRD pattern corresponds to a different crystal facet of materials,[51,112] and its relative peak intensity has a positive relationship with the extent of crystal facet exposure.[50,55] For instance, in the XRD pattern of MnO_2 with different exposed surfaces (Fig. 4(B)), the peak intensity corresponding to the (110) surface was the strongest among the diffraction peaks in (310), (110), and (100) when MnO_2 was mainly exposed with the (110) surface.[119] Chan *et al.* also reported that the variation of peak intensity of the (104) peak and (110) peak in the XRD pattern of α-Fe_2O_3 rhombohedra, hexagonal bipyramids, and hexagonal nanoplates can be ascribed to the morphology transformation.[38] However, it should be noted that it is inaccurate to determine the exposed surface of materials by XRD analysis alone, and it is usually required to combine with TEM analysis.

3.2 Characterization techniques for defects

As mentioned earlier, the defects in Fe catalysts are generally classified into two main categories, that is, dopants and vacancies. For dopants, the corresponding X-ray photoelectron spectrometry (XPS) spectrum, Fourier transform infrared spectra (FTIR) spectra, and Energy dispersive X-ray (EDX) mapping can be used to verify their existence through clarifying the element composition and chemical bond.[117,118,128]

In the case of vacancies, XPS is a common technology to demonstrate their existence in nanomaterials since the generated vacancies usually lead to the change of chemical environments of the corresponding elements, which can be reflected by XPS peaks.[69,129] Taking oxygen vacancies as an example, Zhang *et al.* reported that the O 1s XPS spectrum of Co doped $ZnFe_2O_4$ can be divided to two peaks including lattice oxygen (529.6 eV) and surface oxygen (530.9 eV). After Co doping, the lattice oxygen peak intensity of $ZnFe_{0.8}Co_{0.4}O_{2.4}$ obviously decreased and the corresponding binging energy shifted by 0.3 eV in comparison with pure $ZnFe_2O_4$ (Fig. 4(C)), indicating the formation of oxygen vacancies.[120] This phenomenon can also be found in the O 1s spectrum of Ca–Fe_2O_3, hollow sphere $CuFe_2O_4$,[11] Fe_3O_4,[130] and alkylpolyglycoside modified $MnFe_2O_4$.[131]

Meanwhile, X-ray absorption spectroscopy (XAS) based on synchrotron radiation has emerged as another crucial approach to directly identify the existence of vacancies in materials.[120,132] XAS can study the local atomic structure in a material, such as the changes in electronic structures and geometry, which can be classified into X-ray absorption near edge structure (XANES) and extended X-ray absorption fine structure (EXAFS) depending on the absorption energies, in which XANES usually provides information about the oxidation state of the absorbing atom, and EXAFS generally determines the local bonding environments of the absorbing atom, such as the atomic coordination number and interatomic distance.[133,134] Typically, as revealed by the Fourier transform (FT) EXAFS spectra at the W L_3-edge, defect-rich WO_3 (R-WO_3) showed shifted peaks and lower peak intensities in comparison with commercial WO_3 (C-WO_3) and defect-deficient WO_3 (D-WO_3), manifesting their distinguishing local atomic arrangements (Fig. 4(D)). Besides, R-WO_3 displayed a reduced coordination number compared to C-WO_3 and D-WO_3, which demonstrated that abundant oxygen vacancies were formed in R-WO_3.[135] Xiao *et al.* also compared the coordination number of Co in pure Co_3O_4 and Co_3O_4 etched with Ar plasma (V_o-Co_3O_4) *via* observing the FT-EXAFS spectra at the Co k-edge, where a relatively lower coordination number was found in the latter, indicating the creation of oxygen vacancies after etching Co_3O_4 with Ar plasma. In addition, by studying the Co K-edge XANES spectra, it was found that the Co valence in V_o-Co_3O_4 decreased compared to pure Co_3O_4, further identifying the existence of oxygen vacancies in V_o-Co_3O_4.[123]

Besides the above technologies, electron paramagnetic resonance (EPR) characterization is also a common approach to verify the vacancy in materials since there are usually some unpaired electrons around the vacancy.[124,129,136] Moreover, it is also possible to compare the concentration of vacancies by studying the change of the EPR signal.[124] For example, Wu *et al.* found that all Fe–Co LDH samples prepared with different precursor proportions showed EPR signals with a *g* value of 2.002, demonstrating the presence of oxygen vacancies. Besides, the EPR intensities varied when the content of the Fe precursor increased, which revealed the variation of the number of oxygen vacancies (Fig. 4(E)).[71] Liu *et al.* also verified the existence of sulfur vacancies in Fe_3S_4 by EPR technology with a *g* value of 2.005.[80]

3.3 Characterization techniques for the catalyst size

As common technologies to observe the morphology of materials, SEM and TEM characterization techniques have been widely employed to study the approximate size of catalysts.[50,55,137] For example, it can be observed from Fig. 5(A) that the α-Fe_2O_3 rhombohedron exhibited uniform size with an edge of about 50 nm.[46] Nevertheless, the resolution of conventional SEM and TEM technologies at the nanoscale cannot provide information at the atomic scale. For more detailed information about SACs, some other characterization techniques such as aberration-corrected high-angle annular dark-field imaging scanning TEM (HAADF-STEM), scanning tunneling microscopy (STM), and XAS are further required.[81,87,113]

To be specific, HAADF-STEM can provide visual confirmation of the spatial distribution and location of single metal

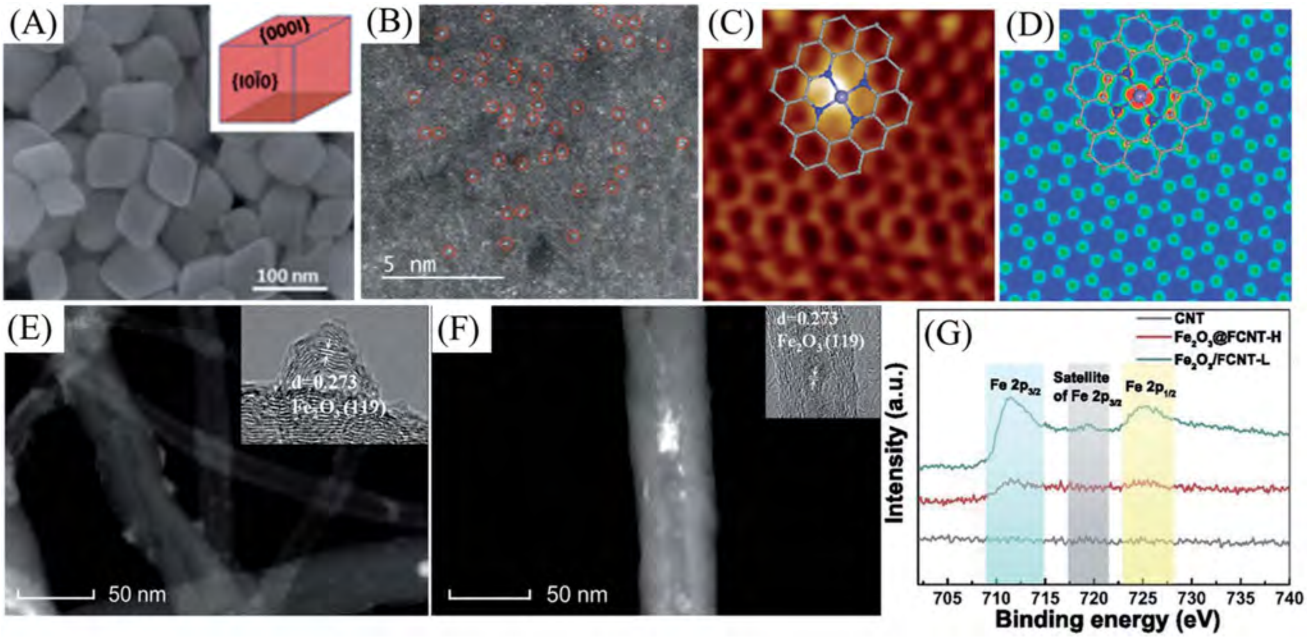

Fig. 5 (A) SEM images of an α-Fe_2O_3 rhombohedron with exposed (0001) and (10$\bar{1}$0) facets. Reprinted with permission from ref. 46, Copyright 2013, Royal Society of Chemistry; (B) the enlarged HAADF-STEM image of Fe SA/NPCs. Reprinted with permission from ref. 113, Copyright 2022, Wiley; (C) low-temperature STM image of FeN_4/GN-2.7 and (D) simulated STM image for (C). The inseted schematic structures represent the structure of graphene-embedded FeN_4. The gray, blue, and light blue balls represent C, N, and Fe atoms, respectively. Reprinted with permission from ref. 115, Copyright 2015, American Association for the Advancement of Science; (E) HADDF-STEM image of Fe_2O_3-out-CNT and (F) Fe_2O_3-int-CNT (inset shows the HRTEM image of the Fe_2O_3 nanoparticle). Reprinted with permission from ref. 109, Copyright 2021, American Chemical Society; (G) Fe 2p XPS spectra of CNTs, Fe_2O_3/FCNT-L and Fe_2O_3@FCNT-H. Reprinted with permission from ref. 110, Copyright 2019, PNAS.

atoms over the catalyst surface owing to its resolution in the sub-angstrom scale, thereby identifying individual atoms.[87,89,97] For example, the distribution of isolated Fe atoms over the carbon surface can be directly observed from enlarged HAADF-STEM images of N-doped porous carbon anchored single Fe atoms (Fe SA/NPCs) (Fig. 5(B)).[113]

As another surface analytical technology that enables imaging of the morphology of surfaces and mapping of the distribution of electronic density, STM has also been employed for characterizing SACs with a two-dimensional structure.[114–116] Furthermore, theoretical simulation based on STM images could provide more detailed information about the atomic sites and change of electronic structures.[81] Taking a graphene confined single iron catalyst (FeN_4/GN) as an example, the simulated STM images in Fig. 5(D) showed that the C and N atoms adjacent to the Fe center were electronically richer compared to C atoms located farther away, which was consistent with the obtained low-temperature STM image (Fig. 5(C)), where the Fe center was resolved as a bright spot, and the neighboring atoms appeared brighter than other C atoms of the graphene matrix.[115]

XAS has also been a common technology to identify single metal atoms in recent studies.[121,122] In general, no metal–metal bonds are formed in the structure of SACs, which can be reflected by the bonding information (*i.e.*, bond length and coordination number) obtained from EXAFS fitting results.[81,86,89] For example, the FT-EXAFS fitting curves of Fe SA/nitrogen-doped porous carbon showed a dominant peak at approximately 1.5 Å, corresponding to the Fe–N scattering paths. Besides, the Fe–Fe peak at ~2.2 Å was not found. Moreover, the fitting results also revealed that the coordination number of Fe was about 4.4, which indicated the presence of Fe–N_4 coordination with some wobbling effect of a fifth ligand.[113] In addition, the valence state of single metal atoms can be revealed by XANES analysis.[113,122]

3.4 Characterization techniques for nanoconfinement

In general, SEM and TEM characterization may provide useful information to confirm the specific nanoconfinement through showing the distribution of particles.[138,139] For example, The SEM and TEM images of FeCu–N/C confirmed the distribution of some metal nanoparticles at the top and inner walls of CNTs.[111] The HAADF-STEM images of Fe_2O_3-in-CNT and Fe_2O_3-out-CNT also clearly showed that Fe_2O_3 distributed inside and outside CNTs, respectively (Fig. 5(E and F)).[109] Besides, N_2 adsorption–desorption isotherms, which are generally employed to investigate the pore characteristics and specific surface areas of a material,[140] can also confirm the spatial nanoconfinement of nanoparticles. In general, confining nanoparticles in the internal pores of porous materials probably leads to the decrease of the Brunner–Emmet–Teller (BET) surface area and pore volume owing to the part blockage of the pore system.[141,142] For example, the confinement of Pd/PdO/Fe_2O_3 nanoparticles in SBA-15 was probed by the variation of the pore volume and BET surface area. The results indicated that pure SBA-15 and FePd-SBA showed a similar hexagonal pore structure, while the pore volume and surface area decreased from 0.94 $cm^3\ g^{-1}$ and 558 $m^2\ g^{-1}$ for pure SBA-15 to 0.55 $cm^3\ g^{-1}$ and 369 $m^2\ g^{-1}$ for FePd-SBA, respectively, which could be ascribed to the successful incorporation of FePd nanoparticles inside SBA-15 pore channels.[125] Lu *et al.* also revealed the lower BET surface area and pore volume of γ-Fe_2O_3/ordered mesoporous carbon in comparison with bare ordered mesoporous carbon, which can be related to the immobilization of γ-Fe_2O_3 into the pore system.[126]

Apart from the above technologies, the confinement of nanoparticles may also be proved by XPS, since XPS is a surface analysis method which can obtain information from the surface at a depth of about 3–5 nm.[102,143] For example, Yang *et al.* found that the mass fractions of Fe_2O_3 in Fe_2O_3/FCNT-H (Fe_2O_3 anchored inside CNTs for nanoconfinement) and Fe_2O_3/FCNT-L (Fe_2O_3 dispersed on the outer surface of CNTs) were detected to be similar, while the peak intensity of Fe 2p for Fe_2O_3/FCNT-H was much lower than that for Fe_2O_3/FCNT-L (Fig. 5(G)), which was possibly because the limited probe depth of the photoelectrons made it difficult to detect the Fe_2O_3 inside the CNT.[110]

4. Structural design of iron catalysts

After fully understanding the impacts of the structural properties on the Fenton-like catalytic performance and technologies to determine the structure–activity relationship, we will then focus on the methods to prepare Fe catalysts with a specific structure. Generally speaking, the catalyst structures will be greatly affected by the changes of synthesis parameters, such as temperature, solvent, and precursor. Therefore, in this section, we review some frequently used strategies for modulating the exposed surface, creating defects, adjusting the catalyst size, and designing a nanoconfined environment, which is significant for endowing Fe catalysts with desirable Fenton-like catalytic properties.

4.1 Design of exposed surfaces

For preparing Fe catalysts with a well-defined special surface, many efforts have been devoted. Generally, the final exposed surface of crystals is intrinsically determined by the growth rate and orientation of seeds that are related to the interplay between growing thermodynamics and kinetics.[144,145] Under thermodynamic control, the greatest proportion of the produced product will be the most stable product, that is, the final crystal is generally enclosed by the surface possessing low surface energy to minimize the total surface energy of crystals, and keep the crystal in an equilibrium shape.[119,146] Meanwhile the surfaces with high surface energy are likely to vanish in the crystal owing to the fast growth rate.

In contrast, the relative growth rate of different surfaces could be regulated under kinetic control, such as changing the synthesis parameters or using morphology-capping agents (*i.e.*, oxalic acid, hydrofluoric acid, and phosphate ions),[50,146,147] and thus, it is possible to synthesize the same crystal with different exposed surfaces. For example, Fe_3O_4 nanoparticles with different exposed surfaces, namely, nanocubes with a (100)

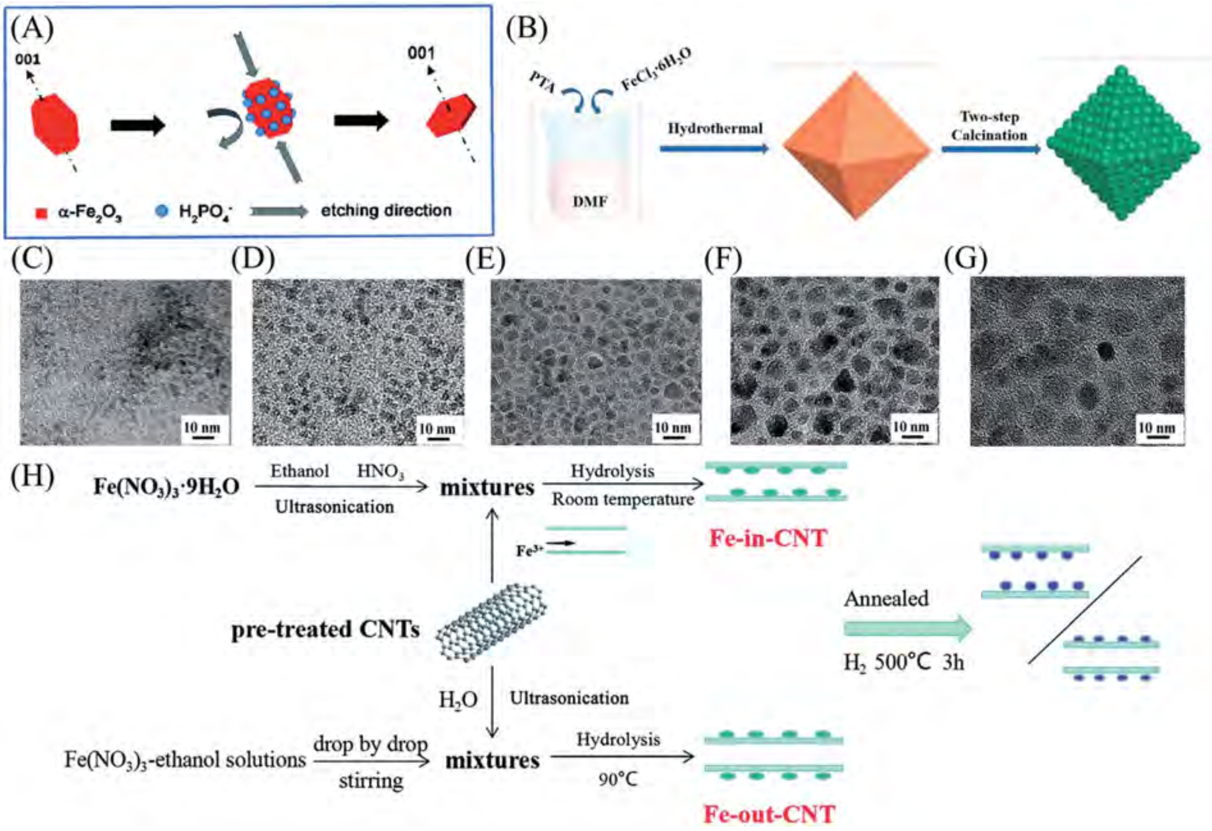

Fig. 6 (A) Schematic illustration of the etching process. Reprinted with permission from ref. 149, Copyright 2010, American Chemical Society; (B) schematic representation of the preparation process of oxygen deficient α-Fe_2O_3. Reprinted with permission from ref. 154, Copyright 2020, Elsevier; TEM images of size-defined γ-Fe_2O_3: (C) γ-Fe_2O_3-130, (D) γ-Fe_2O_3-180, (E) γ-Fe_2O_3-200, (F) γ-Fe_2O_3-230, and (G) γ-Fe_2O_3-250. Reprinted with permission from ref. 164, Copyright 2010, Elsevier. (H) Experimental diagram showing the preparation of Fe0-in-CNT and Fe0-out-CNT. Reprinted with permission from ref. 171, Copyright 2019, Royal Society of Chemistry.

surface and rhombicuboctahedra with both (100) and (110) surfaces, were synthesized by controlling the concentration of the precursor or the injection rate of the precursor.[148] In another study, phosphate ions ($H_2PO_4^-$) as morphology capping agents could allow the etching to proceed along the (001) direction through adsorbing on the (110) planes of α-Fe_2O_3 crystals, thereby acquiring α-Fe_2O_3 nanodiscs with major (001) facets and minor (110) facets (Fig. 6(A)).[149] It is worth noting that the selection of morphology-capping agents is crucial to control the surface energies and surface growth in the crystal due to their reaction with specific surfaces. Theoretically studying the variation of the surface energy of a surface before and after adsorbing morphology-capping agents may provide a promising opportunity for choosing an appropriate morphology-capping agent to synthesize crystalline Fe catalysts with the target surface,[54,150] which needs more research focus in the future.

4.2 Design of defects

As previously mentioned, dopants and vacancies are the two major defects in Fe catalysts. For preparing Fe catalysts with dopants, the raw materials of dopants and Fe catalysts are generally mixed homogeneously to form a precursor, followed by hydrothermal or calcination treatment of the precursor to form doped Fe catalysts.[62,64,117]

For preparing Fe catalysts with oxygen vacancies, various methods including thermal treatment, element doping, and reduction processing have been developed.[68,124,151] Among them, thermal treatment has been widely applied. It is demonstrated that calcining Fe catalysts in an inert or vacuum atmosphere at high temperature could result in the removal of lattice oxygen without phase transformation, leading to the generation of oxygen vacancies. For example, plentiful oxygen vacancies could be introduced into $LaFeO_3$ through annealing $LaFeO_3$ in a hydrogen atmosphere (0.95 bar), and the oxygen vacancy concentration increased with increasing the annealing temperature.[152] Moreover, Ling *et al.* found that oxygen vacancies could be created on hematite by sintering hematite under an oxygen-deficient atmosphere (the mixture of N_2 and air). Besides, the oxygen content during thermal treatment prominently influenced the production of oxygen vacancies.[153] In another case, Xiong *et al.* synthesized an α-Fe_2O_3 nano-octahedron with oxygen vacancies through two-step calcination of the Fe-MOF precursor. During the calculation process, Fe-MOF was firstly oxidized to α-Fe_2O_3 under an air atmosphere, and α-Fe_2O_3 with oxygen vacancies was obtained by further calcining the obtained α-Fe_2O_3 under a nitrogen atmosphere (Fig. 6(B)).[154]

Besides that, element doping is also considered to be an effective technology for introducing oxygen vacancies into Fe catalysts. Many literature studies have reported that the oxygen vacancies could be formed *via* doping metal ions with lower oxidation states due to a charge compensation effect, and the mechanism can be explained by eqn (3).[68,155,156] For instance, in Xie *et al.*'s work of using Cu-doped $Fe_3O_4@\gamma\text{-}Al_2O_3$ to initiate a Fenton-like reaction, the substitution of Fe^{3+}/Al^{3+} by low-valent Cu^{2+} could lead to metal valence state transformation, and oxygen vacancies were generated to meet the charge balance requirement, which benefited the activation of H_2O_2 to generate $^{\bullet}OH$.[157] In another case, Zhao *et al.* prepared a novel nickel-substituted $AgFeO_2$ ($AgFe_{1-x}Ni_xO_2$) catalyst with controlled oxygen vacancies through a hydrothermal method. The results demonstrated that Ni^{2+} with a lower valence substituted the Fe^{3+} in the B-site of the delafossite structure, and therefore led to the generation of abundant oxygen vacancies.[156] Zhao *et al.* also found that the increased concentration of oxygen vacancies in the Fe/CeO_2 composite could be ascribed to the substitution of framework Ce^{4+} by Fe^{3+} with a lower oxidation state.[158] In addition, doping metal ions with a larger atomic radius may also lead to the generation of oxygen vacancies. As literature reported, doping metal ions with a much larger atomic radius might cause the partial replacement of strongly bound oxygen by relatively weakly bound oxygen, which tended to release into solution and form oxygen vacancies.[64,159] For example, Tian *et al.* revealed that doping Ce into 3D Mn_2O_3 could successfully increase the concentration of oxygen vacancies because of the much larger atomic radius of Ce in comparison with Mn.[159]

$$2A^{n+}O \xrightarrow{B^{(n-1)+}O} 2A'_B + V_O^{\bullet\bullet} + 2O_O^{\times} \qquad (3)$$

where A represents the bulk metal ions, B represents the doped metal ions, the superscript × represents the nominal neutral charge, ′ represents the nominal negative charge, and $^{\bullet}$ represents the nominal positive charge.

Some reports show that using reducing agents such as $NaBH_4$ during the synthetic process can also introduce oxygen vacancies into Fe catalysts, and the mechanism is related to the charge neutralization arising from the decreased oxidation state of Fe during redox cycles.[76] For example, $(Co, Fe)_3O_4$/carbon cloth with massive oxygen vacancies was synthesized *via* immersing the obtained $(Co, Fe)_3O_4$/carbon cloth in a $NaBH_4$ solution for a period.[160] Yan *et al.* pointed out that treating the pristine $CoFe_2O_4$ hollow nanosphere with $NaBH_4$ solution could produce abundant oxygen vacancies on the $CoFe_2O_4$ surface.[161] Besides, the presence of reducing agents may also modulate the generation of sulfur vacancies. As some studies reported the concentration of sulfur vacancies in Fe_3S_4 can be adjusted by altering the ratio of ethylene glycol to water during the synthesis process.[80,162]

4.3 Design of the catalyst size

The size of the catalyst can usually be modulated by changing the synthesis parameters (*i.e.*, the ratio of precursors, pH of the growth solution, reaction temperature and reaction time).[52,55,163] For example, $\gamma\text{-}Fe_2O_3$ with catalyst size from 2.0 to 12.0 nm was synthesized *via* increasing the solvothermal temperature from 130 to 250 °C (Fig. 6(C–G)).[164] In another case of microwave-assisted synthesis of Fe_3O_4, the particle size of Fe_3O_4 also changed when varying the microwave irradiation time.[55]

While for synthesizing SACs, it is paramount to limit the migration of isolated single atoms on support materials. Many corresponding strategies such as constructing defects to trap metal precursors to stabilize isolated metal atoms,[165] employing molecular-scale pores of porous materials (*i.e.*, covalent-organic frameworks and MOFs) as cages to confine metal species and anchor single metal atoms,[82,86] using coordinating atoms with lone pairs of electrons, for instance, S, N, and O on support materials to bind metal precursors and stabilize single metal atoms,[97,166] and freezing a homogeneous solution of metal precursors to limit the thermal motion of metal species[167] have thus been proposed in the field of SAC synthesis. Recently, some studies also proposed that pyrolyzing organic-Fe rich biomass, such as Spirulina and Enteromorpha, is possible to generate carbon-based SACs because of the presence of Fe–S or Fe–N bonds in their component,[168–170] which provides a facile and practical strategy for preparing SACs. Nevertheless, improving the metal loading content is still challenging in the field of SAC synthesis although the loading number of single metal atoms is usually positively correlated with their catalytic activity. Increasing the metal atom loading while avoiding the agglomeration arising from their high surface energy and high reactivity needs to be further resolved.

4.4 Design of the nanoconfined environment

In view of the particular advantages of the nanoconfinement effect for Fenton-like processes, most efforts have also been devoted to preparing nanoconfined Fe catalysts. Diverse porous scaffolds with varying material composition such as carbon materials (*i.e.*, CNTs and mesoporous carbon),[171,172] metal oxides (*i.e.*, TiO_2 and anodized aluminum oxide),[173,174] natural minerals (*i.e.*, montmorillonite),[175] MOFs,[176] ceramic ultrafiltration membranes,[106] and silica,[125,177] have been widely employed to encapsulate Fe oxides, zero-valent Fe or Fe complexes to provide a nanoconfined environment through the formation of core@tube, core@shell, mesoporous or lamellar structures. Generally, the hard-template method, soft-template method, and ship-in-a-bottle method are normally used for preparing core@shell structures.[178] The other three structures could be realized by immersing scaffolds with nanotube, mesoporous, or lamellar structures into Fe precursors, followed by calcination or centrifugation.

However, Fe ions may exist on both external and internal surfaces of scaffolds, and driving the diffusion of Fe ions into the nanoconfined channel of scaffolds should be taken into consideration in the process of preparing nanoconfined Fe catalysts. Wang *et al.* proposed a vacuum-assisted impregnation method for synthesizing a TiO_2 nanotube confined Fe_2O_3 catalyst, in which the titanate nanotubes were added into $Fe(NO_3)_3$ aqueous solution and stirred under a vacuum atmosphere ($p <$ 0.01 Pa). In this case, the capillary effect that drived the precursor solution into the internal pores of titanate nanotubes could be strengthened.[179] In another study of synthesizing Fe^0-in-CNTs, Su *et al.* promoted the diffusion of Fe ions into the nanoconfined channel through altering the precursors, reaction temperature and time (Fig. 6(H)).[171] All of these research studies provide useful guidance for further development of confined Fe catalysts.

5. Summary and prospects

Until now, heterogeneous Fenton-like processes have been widely applied in wastewater treatment. Meanwhile, the non-toxicity of Fe, rich source of Fe, and structural flexibility of Fe catalysts have created many opportunities for actual applications. In this case, heterogeneous Fenton-like processes based on Fe catalysts have attracted considerable attention. However, the negative effects related to the excessive use of H_2O_2 should not be overlooked. Therefore, it becomes more significant to understand structure–activity relationships to improve H_2O_2 utilization and reduce the consumption of H_2O_2 for environmentally sustainable applications. In this review, we mainly focus on the fundamental and experimental advances in the structural design of Fe catalysts for modulating the atomic and electronic structures to enhance Fenton-like performance. To be specific, modulating the structural properties of Fe catalysts (exposed facet, defects, catalyst size, and space confinement) is possible to facilitate the exposure of active sites, increase the electron density around active sites, alter the coordination number, promote charge transfer or minimize the mass transfer limitation, and therefore boost the Fenton-like reaction. Besides, some characterization technologies for evaluating the achievements of structural design and synthetic strategies to design Fe catalysts with a specific structure are also summarized. Based on the current studies, the existing challenges and further research suggestions are proposed.

Firstly, except for enhancing H_2O_2 utilization to reduce its consumption, the structural design of Fe catalysts may also lead to the change of the reaction mechanism, for example, the varied contribution of the radical pathway and nonradical pathway. Therefore, it is worth studying the effects of structural design on the catalytic mechanism. The obtained details may shed new light on Fe-based Fenton-like reactions.

Secondly, it is essential to understand the link between the structural properties of Fe catalysts and their synthesis conditions more precisely. As described in this manuscript, a number of methods have been successfully employed to design the exposed surface, defects, catalyst size, and nanoconfined environment, while structural design in a controllable manner remains a great challenge. To this end, the formation mechanisms of these structural properties need more elucidation, so as to achieve controllable synthesis of Fe catalysts with specific structures.

Thirdly, the nature of the mentioned four structural properties that affect Fenton-like performance could be attributed to the variation of catalyst atomic and electronic structures, which have a significant influence on the interaction between catalysts and H_2O_2. Therefore, in addition to these structural properties, other modification strategies that can optimize the coordination number, electron distribution and charge transfer can also be developed for the construction of highly efficient Fe catalysts.

Fourthly, some other metal-based catalysts, for instance, Cu catalysts, Mn catalysts, Co catalysts, *etc.*, are also widely used in heterogeneous Fenton-like systems for organic pollutant degradation. The mentioned structural design strategies in this review can also be applied to design other metal catalysts for acquiring enhanced Fenton-like catalytic activity, thus promoting the development of environmentally friendly and sustainable materials for wastewater treatment.

Conflicts of interest

There are no conflicts to declare.

Acknowledgements

This study was financially supported by the Program for the National Natural Science Foundation of China (U20A20323, 51521006, 51779090, 52170161, 51879101, 51579098, 51709101, 51809090, and 51909084), the National Program for Support of Top-Notch Young Professionals of China (2014), the Program for Changjiang Scholars and Innovative Research Team in University (IRT-13R17), and the Hunan Natural Science Foundation (2020JJ3009), the Hunan Researcher Award Program (2020RC3025), the Hunan Provincial Science and Technology Plan Project (2018SK20410, 2017SK2243, and 2016RS3026), the Fundamental Research Funds for the Central Universities (531118010247 and 531118040083), and the Science and Technology Innovation Program of Hunan Province (2021RC2057).

References

1 L. Qin, Z. Wang, Y. Fu, C. Lai, X. Liu, B. Li, S. Liu, H. Yi, L. Li, M. Zhang, Z. Li, W. Cao and Q. Niu, *J. Hazard. Mater.*, 2021, **414**, 125448.

2 C. Lai, Z. An, H. Yi, X. Huo, L. Qin, X. Liu, B. Li, M. Zhang, S. Liu, L. Li, Y. Fu, X. Zhou, Z. Wang, N. An and X. Shi, *J. Colloid Interface Sci.*, 2021, **600**, 161–173.

3 B. Li, S. Yu, M. Zhou, C. Chen, C. Lai, M. Zhang and H. Lin, *J. Mater. Chem. A*, 2022, **10**, 3905–3932.

4 J. He, C. Lai, L. Qin, B. Li, S. Liu, L. Jiao, Y. Fu, D. Huang, L. Li, M. Zhang, X. Liu, H. Yi, L. Chen and Z. Li, *Chemosphere*, 2020, **256**, 127083.

5 L. Jiang, Y. Liu, S. Liu, G. Zeng, X. Hu, X. Hu, Z. Guo, X. Tan, L. Wang and Z. Wu, *Environ. Sci. Technol.*, 2017, **51**, 6352–6359.

6 C. He, W. Xia, C. Zhou, D. Huang, C. Zhang, B. Song, Y. Yang, J. Li, X. Xu, Y. Shang and L. Du, *Chem. Eng. J.*, 2022, **430**, 132751.

7 M. Zhang, C. Lai, B. Li, F. Xu, D. Huang, S. Liu, L. Qin, Y. Fu, X. Liu, H. Yi, Y. Zhang, J. He and L. Chen, *Chem. Eng. J.*, 2020, **396**, 125343.

8 B. Li, C. Lai, H. Lin, S. Liu, L. Qin, M. Zhang, M. Zhou, L. Li, H. Yi and L. Chen, *Chem. Eng. J.*, 2022, **431**, 134044.

9 Y. Fu, Z. Yin, L. Qin, D. Huang, H. Yi, X. Liu, S. Liu, M. Zhang, B. Li, L. Li, W. Wang, X. Zhou, Y. Li, G. Zeng and C. Lai, *J. Hazard. Mater.*, 2022, **422**, 126950.
10 H. Yan, C. Lai, D. Wang, S. Liu, X. Li, X. Zhou, H. Yi, B. Li, M. Zhang, L. Li, X. Liu, L. Qin and Y. Fu, *J. Mater. Chem. A*, 2021, **9**, 11944–11960.
11 R.-R. Ding, W.-Q. Li, C.-S. He, Y.-R. Wang, X.-C. Liu, G.-N. Zhou and Y. Mu, *Appl. Catal., B*, 2021, **291**, 120069.
12 X. Wang, X. Zhang, Y. Zhang, Y. Wang, S.-P. Sun, W. D. Wu and Z. Wu, *J. Mater. Chem. A*, 2020, **8**, 15513–15546.
13 D. Ma, H. Yi, C. Lai, X. Liu, X. Huo, Z. An, L. Li, Y. Fu, B. Li, M. Zhang, L. Qin, S. Liu and L. Yang, *Chemosphere*, 2021, **275**, 130104.
14 L. Li, C. Lai, F. Huang, M. Cheng, G. Zeng, D. Huang, B. Li, S. Liu, M. Zhang, L. Qin, M. Li, J. He, Y. Zhang and L. Chen, *Water Res.*, 2019, **160**, 238–248.
15 J. Wang, C. Liu, J. Feng, D. Cheng, C. Zhang, Y. Yao, Z. Gu, W. Hu, J. Wan and C. Yu, *J. Hazard. Mater.*, 2020, **394**, 122567.
16 Y. Zhong, X. Liang, Z. He, W. Tan, J. Zhu, P. Yuan, R. Zhu and H. He, *Appl. Catal., B*, 2014, **150–151**, 612–618.
17 J. Wang and J. Tang, *J. Mol. Liq.*, 2021, **332**, 115755.
18 M. Munoz, Z. M. de Pedro, J. A. Casas and J. J. Rodriguez, *Appl. Catal., B*, 2015, **176–177**, 249–265.
19 H. Barndõk, L. Blanco, D. Hermosilla and Á. Blanco, *Chem. Eng. J.*, 2016, **284**, 112–121.
20 B. Yang, P. Zhou, X. Cheng, H. Li, X. Huo and Y. Zhang, *J. Colloid Interface Sci.*, 2019, **555**, 383–393.
21 Z. Wang, C. Lai, L. Qin, Y. Fu, J. He, D. Huang, B. Li, M. Zhang, S. Liu, L. Li, W. Zhang, H. Yi, X. Liu and X. Zhou, *Chem. Eng. J.*, 2020, **392**, 124851.
22 G. Wang, D. Zhao, F. Kou, Q. Ouyang, J. Chen and Z. Fang, *Chem. Eng. J.*, 2018, **351**, 747–755.
23 J. Gao, Y. Liu, X. Xia, L. Wang and W. Dong, *J. Hazard. Mater.*, 2018, **353**, 393–400.
24 Z. Zhao, S. Pan, Y. Ye, X. Zhang and B. Pan, *Chem. Eng. J.*, 2020, **381**, 122667.
25 H. Wang, M. Jing, Y. Wu, W. Chen and Y. Ran, *J. Hazard. Mater.*, 2018, **353**, 53–61.
26 J. Bai, Y. Liu, X. Yin, H. Duan and J. Ma, *Appl. Surf. Sci.*, 2017, **416**, 45–50.
27 Y. Liu, H. Cheng, M. Cheng, Z. Liu, D. Huang, G. Zhang, B. Shao, Q. Liang, S. Luo, T. Wu and S. Xiao, *Chem. Eng. J.*, 2020, **417**, 127914.
28 L. Lyu, L. Zhang, G. He, H. He and C. Hu, *J. Mater. Chem. A*, 2017, **5**, 7153–7164.
29 X. Hou, X. Huang, F. Jia, Z. Ai, J. Zhao and L. Zhang, *Environ. Sci. Technol.*, 2017, **51**, 5118–5126.
30 X. Huang, Y. Chen, E. Walter, M. Zong, Y. Wang, X. Zhang, O. Qafoku, Z. Wang and K. M. Rosso, *Environ. Sci. Technol.*, 2019, **53**, 10197–10207.
31 Y. Zhu, R. Zhu, Y. Xi, J. Zhu, G. Zhu and H. He, *Appl. Catal., B*, 2019, **255**, 117739.
32 X. Wei, H. Yi, C. Lai, X. Huo, D. Ma and C. Du, *J. Colloid Interface Sci.*, 2022, **608**, 942–953.
33 T. Yang, D. Yu, D. Wang, T. Yang, Z. Li, M. Wu, M. Petru and J. Crittenden, *Appl. Catal., B*, 2021, **286**, 119859.
34 M. Ahmad, X. Quan, S. Chen and H. Yu, *Appl. Catal., B*, 2020, **264**, 118534.
35 X. Huang, X. Hou, F. Jia, F. Song, J. Zhao and L. Zhang, *ACS Appl. Mater. Interfaces*, 2017, **9**, 8751–8758.
36 Z. W. Chen, L. X. Chen, C. C. Yang and Q. Jiang, *J. Mater. Chem. A*, 2019, **7**, 3492–3515.
37 X.-F. Yang, A. Wang, B. Qiao, J. Li, J. Liu and T. Zhang, *Acc. Chem. Res.*, 2013, **46**, 1740–1748.
38 J. Y. T. Chan, S. Y. Ang, E. Y. Ye, M. Sullivan, J. Zhang and M. Lin, *Phys. Chem. Chem. Phys.*, 2015, **17**, 25333–25341.
39 J. Zan, H. Song, S. Zuo, X. Chen, D. Xia and D. Li, *J. Cleaner Prod.*, 2020, **246**, 118971.
40 H. Jin, X. Tian, Y. Nie, Z. Zhou, C. Yang, Y. Li and L. Lu, *Environ. Sci. Technol.*, 2017, **51**, 12699–12706.
41 K. Pan, C. Yang, J. Hu, W. Yang, B. Liu, J. Yang, S. Liang, K. Xiao and H. Hou, *J. Hazard. Mater.*, 2020, **389**, 122072.
42 N. Thomas, D. D. Dionysiou and S. C. Pillai, *J. Hazard. Mater.*, 2021, **404**, 124082.
43 N. Farhadian, S. Liu, A. Asadi, M. Shahlaei and S. Moradi, *J. Mol. Liq.*, 2021, **321**, 114896.
44 J. Wang and J. Tang, *Chemosphere*, 2021, **276**, 130177.
45 S. D. Taylor, L. Kovarik, J. B. Cliff and K. M. Rosso, *Environ. Sci.: Nano*, 2019, **6**, 2429–2440.
46 Y. Zhao, F. Pan, H. Li, T. Niu, G. Xu and W. Chen, *J. Mater. Chem. A*, 2013, **1**, 7242–7246.
47 M. Qin, B. Lu, S. Feng, Z. Zhen, R. Chen and H. Liu, *Chemosphere*, 2019, **230**, 286–293.
48 S.-S. Lin and M. D. Gurol, *Environ. Sci. Technol.*, 1998, **32**, 1417–1423.
49 C. M. Lousada, A. J. Johansson, T. Brinck and M. Jonsson, *J. Phys. Chem. C*, 2012, **116**, 9533–9543.
50 X. Liao, F. Wang, F. Wang, Y. Cai, Y. Yao, B.-T. Teng, Q. Hao and L. Shuxiang, *Appl. Catal., B*, 2019, **259**, 118064.
51 M. Zong, D. Song, X. Zhang, X. Huang, X. Lu and K. M. Rosso, *Environ. Sci. Technol.*, 2021, **55**, 677–688.
52 J. Liu, X. Li, B. Liu, C. Zhao, Z. Kuang, R. Hu, B. Liu, Z. Ao and J. Wang, *ACS Appl. Mater. Interfaces*, 2018, **10**, 38051–38056.
53 C. Dai, X. Tian, N. Yulun, H.-M. Lin and C. Yang, *Environ. Sci. Technol.*, 2018, **52**, 6518–6525.
54 G. Liu, H. G. Yang, J. Pan, Y. Q. Yang, G. Q. Lu and H.-M. Cheng, *Chem. Rev.*, 2014, **114**, 9559–9612.
55 Y. Zhong, L. Yu, Z.-F. Chen, H. He, F. Ye, G. Cheng and Q. Zhang, *ACS Appl. Mater. Interfaces*, 2017, **9**, 29203–29212.
56 Y. Chen, C. J. Miller and T. D. Waite, *Environ. Sci. Technol.*, 2021, **55**, 14414–14425.
57 H. Li, J. Shang, Z. Yang, W. Shen, Z. Ai and L. Zhang, *Environ. Sci. Technol.*, 2017, **51**, 5685–5694.
58 Y. Nosaka and A. Nosaka, *ACS Energy Lett.*, 2016, **1**, 356–359.
59 J. Luo, D. Yu, K. D. Hristovski, K. Fu, Y. Shen, P. Westerhoff and J. C. Crittenden, *Environ. Sci. Technol.*, 2021, **55**, 4287–4304.
60 J. Luo, Y. Liu, C. Fan, L. Tang, S. Yang, M. Liu, M. Wang, C. Feng, X. Ouyang, L. Wang, L. Xu, J. Wang and M. Yan, *ACS Catal.*, 2021, **11**, 11440–11450.
61 A. V. Marenich, C. J. Cramer and D. G. Truhlar, *J. Phys. Chem. B*, 2009, **113**, 6378–6396.

62 J. Deng, C. Ye, A. Cai, L. Huai, S. Zhou, F. Dong, X. Li and X. Ma, *Chem. Eng. J.*, 2021, **420**, 129863.

63 L. Lyu, L. Zhang and C. Hu, *Environ. Sci.: Nano*, 2016, **3**, 1483–1492.

64 S. Guo, H. Wang, W. Yang, H. Fida, L. You and K. Zhou, *Appl. Catal., B*, 2020, **262**, 118250.

65 Y. Gao, W. Zhu, J. Liu, P. Lin, J. Zhang, T. Huang and K. Liu, *Appl. Catal., B*, 2021, **295**, 120273.

66 M. K. Panjwani, Q. Wang, Y. Ma, Y. Lin, F. Xiao and S. Yang, *Environ. Sci.: Nano*, 2021, **8**, 2204–2213.

67 Q. Ji, L. Bi, J. Zhang, H. Cao and X. S. Zhao, *Energy Environ. Sci.*, 2020, **13**, 1408–1428.

68 K. Zhu, F. Shi, X. Zhu and W. Yang, *Nano Energy*, 2020, **73**, 104761.

69 T. Soltani and B.-K. Lee, *J. Mol. Catal. A: Chem.*, 2016, **425**, 199–207.

70 X. X. Guo, T. T. Hu, B. Meng, Y. Sun and Y.-F. Han, *Appl. Catal., B*, 2020, **260**, 118157.

71 L. Wu, J. Hong, Q. Zhang, B.-Y. Chen, J. Wang and Z. Dong, *Chem. Eng. J.*, 2020, **385**, 123620.

72 Y. Bu, H. Li, W. Yu, Y. Pan, L. Li, Y. Wang, L. Pu, J. Ding, G. Gao and B. Pan, *Environ. Sci. Technol.*, 2021, **55**, 2110–2120.

73 S. Zhan, H. Zhang, X. Mi, Y. Zhao, C. Hu and L. Lyu, *Environ. Sci. Technol.*, 2020, **54**, 8333–8343.

74 Y. Wang, P. Zhang, T. Li, L. Lyu, Y. Gao and C. Hu, *J. Hazard. Mater.*, 2021, **408**, 124818.

75 C. Chen, K. Xu, X. Ji, B. Zhang, L. Miao and J. Jiang, *J. Mater. Chem. A*, 2015, **3**, 12461–12467.

76 X. Zhang, X. Liu, Y. Zeng, Y. Tong and X. Lu, *Small Methods*, 2020, **4**, 1900823.

77 W. Wang, Y. Liu, Y. Yue, H. Wang, G. Cheng, C. Gao, C. Chen, Y. Ai, Z. Chen and X. Wang, *ACS Catal.*, 2021, **11**, 11256–11265.

78 C. Zhou, L. Zhu, L. Deng, H. Zhang, H. Zeng and Z. Shi, *Sep. Purif. Technol.*, 2021, **276**, 119404.

79 H. Kuang, Z. He, M. Li, R. Huang, Y. Zhang, X. Xu, L. Wang, Y. Chen and S. Zhao, *Chem. Eng. J.*, 2021, **417**, 127987.

80 W. Liu, J. Tian, C. Mao, Z. Wang, J. Liu, R. A. Dahlgren, L. Zhang and X. Wang, *Anal. Chim. Acta*, 2020, **1127**, 246–255.

81 Y. Shang, X. Xu, B. Gao, S. Wang and X. Duan, *Chem. Soc. Rev.*, 2021, **50**, 5281–5322.

82 Y. Chen, S. Ji, C. Chen, Q. Peng, D. Wang and Y. Li, *Joule*, 2018, **2**, 1242–1264.

83 M. Xu, C. Lai, X. Liu, B. Li, M. Zhang, F. Xu, S. Liu, L. Li, L. Qin, H. Yi and Y. Fu, *J. Mater. Chem. A*, 2021, **9**, 24148–24174.

84 W. Yang, P. Hong, D. Yang, Y. Yang, Z. Wu, C. Xie, J. He, K. Zhang, L. Kong and J. Liu, *J. Colloid Interface Sci.*, 2021, **597**, 56–65.

85 M. Zhang, C. Lai, B. Li, S. Liu, D. Huang, F. Xu, X. Liu, L. Qin, Y. Fu, L. Li, H. Yi and L. Chen, *Small*, 2021, **17**, 2007113.

86 Y. J. Chen, S. F. Ji, Y. G. Wang, J. C. Dong, W. X. Chen, Z. Li, R. A. Shen, L. R. Zheng, Z. B. Zhuang, D. S. Wang and Y. D. Li, *Angew. Chem., Int. Ed.*, 2017, **56**, 6937–6941.

87 Y. Yin, L. Shi, W. Li, X. Li, H. Wu, Z. Ao, W. Tian, S. Liu, S. Wang and H. Sun, *Environ. Sci. Technol.*, 2019, **53**, 11391–11400.

88 Y. Gao, C. Yang, M. Zhou, C. He, S. Cao, Y. Long, S. Li, Y. Lin, P. Zhu and C. Cheng, *Small*, 2020, **16**, 2005060.

89 F. Chen, X.-L. Wu, C. Shi, H. Lin, J. Chen, Y. Shi, S. Wang and X. Duan, *Adv. Funct. Mater.*, 2021, **31**, 2007877.

90 A. Wang, J. Li and T. Zhang, *Nat. Rev. Chem.*, 2018, **2**, 65–81.

91 L. Su, P. Wang, X. Ma, J. Wang and S. Zhan, *Angew. Chem., Int. Ed.*, 2021, **60**, 21261–21266.

92 Y. Gao, X. Duan, B. Li, Q. Jia, Y. Li, X. Fan, F. Zhang, G. Zhang, S. Wang and W. Peng, *J. Mater. Chem. A*, 2021, **9**, 14793–14805.

93 J. Li, L. Zhang, K. Doyle-Davis, R. Li and X. Sun, *Carbon Energy*, 2020, **2**, 488–520.

94 R. Bliem, J. E. S. v. d. Hoeven, J. Hulva, J. Pavelec, O. Gamba, P. E. d. Jongh, M. Schmid, P. Blaha, U. Diebold and G. S. Parkinson, *P. Natl. Acad. Sci.*, 2016, **113**, 8921–8926.

95 A. Han, B. Wang, A. Kumar, Y. Qin, J. Jin, X. Wang, C. Yang, B. Dong, Y. Jia, J. Liu and X. Sun, *Small Methods*, 2019, **3**, 1800471.

96 T. Zhu, Y. Han, S. Liu, B. Yuan, Y. Liu and H. Ma, *Front. Chem.*, 2021, **9**, 717201.

97 S. Zuo, X. Jin, X. Wang, Y. Lu, Q. Zhu, J. Wang, W. Liu, Y. Du and J. Wang, *Appl. Catal., B*, 2021, **282**, 119551.

98 X. Chen, D.-D. Ma, B. Chen, K. Zhang, R. Zou, X.-T. Wu and Q.-L. Zhu, *Appl. Catal., B*, 2020, **267**, 118720.

99 S. Zhang, T. Hedtke, X. Zhou, M. Elimelech and J.-H. Kim, *ACS EST Engg*, 2021, **1**, 706–724.

100 Y. Chen, G. Zhang, H. Liu and J. Qu, *Angew. Chem., Int. Ed.*, 2019, **58**, 8134–8138.

101 M. Zhang, C. Xiao, X. Yan, S. Chen, C. Wang, R. Luo, J. Qi, X. Sun, L. Wang and J. Li, *Environ. Sci. Technol.*, 2020, **54**, 10289–10300.

102 C. Liu, J. Li, J. Qi, J. Wang, R. Luo, J. Shen, X. Sun, W. Han and L. Wang, *ACS Appl. Mater. Interfaces*, 2014, **6**, 13167–13173.

103 J. Qian, X. Gao and B. Pan, *Environ. Sci. Technol.*, 2020, **54**, 8509–8526.

104 P. Su, W. Fu, X. Du, G. Song, Y. Tang and M. Zhou, *Sep. Purif. Technol.*, 2021, **276**, 119232.

105 S. Zhang, M. Sun, T. Hedtke, A. Deshmukh, X. Zhou, S. Weon, M. Elimelech and J.-H. Kim, *Environ. Sci. Technol.*, 2020, **54**, 10868–10875.

106 S. Zhang, T. Hedtke, Q. Zhu, M. Sun, S. Weon, Y. Zhao, E. Stavitski, M. Elimelech and J.-H. Kim, *Environ. Sci. Technol.*, 2021, **55**, 9266–9275.

107 L. Yu, W.-X. Li, X. Pan and X. Bao, *J. Phys. Chem. C*, 2012, **116**, 16461–16466.

108 X. Pan and X. Bao, *Acc. Chem. Res.*, 2011, **44**, 553–562.

109 D. Guo, Y. Liu, H. Ji, C.-C. Wang, B. Chen, C. Shen, F. Li, Y. Wang, P. Lu and W. Liu, *Environ. Sci. Technol.*, 2021, **55**, 4045–4053.

110 Z. Yang, J. Qian, A. Yu and B. Pan, *P. Natl. Acad. Sci.*, 2019, **116**, 6659.

111 B. Wang, L. Xu, G. Liu, Y. Ye, Y. Quan, C. Wang, W. Wei, W. Zhu, C. Xu, H. Li and J. Xia, *J. Alloys Compd.*, 2020, **826**, 154152.

112 J. Li, C. Xiao, K. Wang, Y. Li and G. Zhang, *Environ. Sci. Technol.*, 2019, **53**, 11023–11030.

113 L. Yang, H. Yang, S. Yin, X. Wang, M. Xu, G. Lu, Z. Liu and H. Sun, *Small*, 2022, **18**, 2104941.

114 Q. Liu, Y. Liu, H. Li, L. Li, D. Deng, F. Yang and X. Bao, *Appl. Surf. Sci.*, 2017, **410**, 111–116.

115 D. Deng, X. Chen, L. Yu, X. Wu, Q. Liu, Y. Liu, H. Yang, H. Tian, Y. Hu, P. Du, R. Si, J. Wang, X. Cui, H. Li, J. Xiao, T. Xu, J. Deng, F. Yang, P. N. Duchesne, P. Zhang, J. Zhou, L. Sun, J. Li, X. Pan and X. Bao, *Sci. Adv.*, 2015, **1**, 1500462.

116 X. Li, X. Yang, J. Zhang, Y. Huang and B. Liu, *ACS Catal.*, 2019, **9**, 2521–2531.

117 H. Zheng, J. Bao, Y. Huang, L. Xiang, F. Mehmood, B. Ren, J. Du, M. N. Nadagouda and D. D. Dionysiou, *Appl. Catal., B*, 2019, **259**, 118056.

118 S. Liu, C. Lai, B. Li, X. Liu, X. Zhou, C. Zhang, L. Qin, L. Li, M. Zhang, H. Yi, Y. Fu, H. Yan and L. Chen, *Chem. Eng. J.*, 2022, **427**, 131655.

119 S. Rong, P. Zhang, F. Liu and Y. Yang, *ACS Catal.*, 2018, **8**, 3435–3446.

120 H. Zhang, C. Li, L. Lyu and C. Hu, *Appl. Catal., B*, 2020, **270**, 118874.

121 S. An, G. Zhang, T. Wang, W. Zhang, K. Li, C. Song, J. T. Miller, S. Miao, J. Wang and X. Guo, *ACS Nano*, 2018, **12**, 9441–9450.

122 Y. Gao, Y. Zhu, T. Li, Z. Chen, Q. Jiang, Z. Zhao, X. Liang and C. Hu, *Environ. Sci. Technol.*, 2021, **55**, 8318–8328.

123 Z. Xiao, Y. Wang, Y.-C. Huang, Z. Wei, C.-L. Dong, J. Ma, S. Shen, Y. Li and S. Wang, *Energy Environ. Sci.*, 2017, **10**, 2563–2569.

124 K. Ye, K. Li, Y. Lu, Z. Guo, N. Ni, H. Liu, Y. Huang, H. Ji and P. Wang, *TrAC, Trends Anal. Chem.*, 2019, **116**, 102–108.

125 X. Li, X. Liu, L. Xu, Y. Wen, J. Ma and Z. Wu, *Appl. Catal., B*, 2015, **165**, 79–86.

126 A.-H. Lu, J.-J. Nitz, M. Comotti, C. Weidenthaler, K. Schlichte, C. W. Lehmann, O. Terasaki and F. Schüth, *J. Am. Chem. Soc.*, 2010, **132**, 14152–14162.

127 Y. Jian, T. Yu, Z. Jiang, Y. Yu, M. Douthwaite, J. Liu, R. Albilali and C. He, *ACS Appl. Mater. Interfaces*, 2019, **11**, 11369–11383.

128 X. Zhou, Z. Zeng, G. Zeng, C. Lai, R. Xiao, S. Liu, D. Huang, L. Qin, X. Liu, B. Li, H. Yi, Y. Fu, L. Li, M. Zhang and Z. Wang, *Chem. Eng. J.*, 2020, **401**, 126127.

129 J. Xiong, J. Di, J. X. Xia, W. S. Zhu and H. M. Li, *Adv. Funct. Mater.*, 2018, **28**, 19.

130 D. Lu, B. Jiang, X. Shen, Z. W. LaTurner, C. Wang, X. Chen, X. Xu and L. Zhu, *Chem. Eng. J.*, 2022, **429**, 132164.

131 R. Zhou, S. Liu, F. He, H. Ren and Z. Han, *Chemosphere*, 2021, **285**, 131433.

132 L. Lei, D. Huang, M. Cheng, R. Deng, S. Chen, Y. Chen and W. Wang, *Coord. Chem. Rev.*, 2020, **418**, 213372.

133 A. I. Frenkel, *Chem. Soc. Rev.*, 2012, **41**, 8163–8178.

134 Y. Yang, G. Zeng, D. Huang, C. Zhang, D. He, C. Zhou, W. Wang, W. Xiong, B. Song, H. Yi, S. Ye and X. Ren, *Small*, 2020, **16**, 2001634.

135 N. Zhang, X. Li, H. Ye, S. Chen, H. Ju, D. Liu, Y. Lin, W. Ye, C. Wang, Q. Xu, J. Zhu, L. Song, J. Jiang and Y. Xiong, *J. Am. Chem. Soc.*, 2016, **138**, 8928–8935.

136 L. Li, S. Liu, M. Cheng, C. Lai, G. Zeng, L. Qin, X. Liu, B. Li, W. Zhang, Y. Yi, M. Zhang, Y. Fu, M. Li and M. Long, *J. Hazard. Mater.*, 2021, **406**, 124333.

137 C. Zhou, E. Almatrafi, X. Tang, B. Shao, W. Xia, B. Song, W. Xiong, W. Wang, H. Guo, S. Chen and G. Zeng, *Sep. Purif. Technol.*, 2022, **286**, 120464.

138 W. Wang, W. Zhou, W. Li, X. Xiong, Y. Wang, K. Cheng, J. Kang, Q. Zhang and Y. Wang, *Appl. Catal., B*, 2020, **276**, 119142.

139 L. Zong, X. Chen, S. Dou, K. Fan, Z. Wang, W. Zhang, Y. Du, J. Xu, X. Jia, Q. Zhang, X. Li, Y. Deng, Y. Chen and L. Wang, *Chin. Chem. Lett.*, 2020, **32**, 1121–1126.

140 F. Xu, C. Lai, M. Zhang, B. Li, S. Liu, M. Chen, L. Li, Y. Xu, L. Qin, Y. Fu, X. Liu, H. Yi and X. Yang, *J. Colloid Interface Sci.*, 2021, **601**, 196–208.

141 Z.-j. Wang, Y. Xie and C.-j. Liu, *J. Phys. Chem. C*, 2008, **112**, 19818–19824.

142 Y. Liu, J. Zhang, W. Hou and J.-J. Zhu, *Nanotechnology*, 2008, **19**, 135707.

143 T. Zeng, X. Zhang, S. Wang, H. Niu and Y. Cai, *Environ. Sci. Technol.*, 2015, **49**, 2350–2357.

144 K. Lee, M. Kim and H. Kim, *J. Mater. Chem.*, 2010, **20**, 3791–3798.

145 T. K. Sau and A. L. Rogach, *Adv. Mater.*, 2010, **22**, 1781–1804.

146 K. Zhou and Y. Li, *Angew. Chem., Int. Ed.*, 2012, **51**, 602–613.

147 Z. Niu and Y. Li, *Chem. Mater.*, 2014, **26**, 72–83.

148 C. H. Ho, C. P. Tsai, C. C. Chung, C. Y. Tsai and C. H. Lai, *Chem. Mater.*, 2011, **23**, 1753–1760.

149 J. S. Chen, T. Zhu, X. H. Yang, H. G. Yang and X. W. Lou, *J. Am. Chem. Soc.*, 2010, **132**, 13162–13164.

150 H. G. Yang, C. H. Sun, S. Z. Qiao, J. Zou, G. Liu, S. C. Smith, H. M. Cheng and G. Q. Lu, *Nature*, 2008, **453**, 638–641.

151 Y. Chen, W. Yang, S. Gao, C. Sun and Q. Li, *ACS Appl. Nano Mater.*, 2018, **1**, 3565–3578.

152 J. Shi, Y. Chang, Y. Tang, X. Wang, X. Wang, X. Zhang and J. Cao, *Ceram. Int.*, 2020, **46**, 5315–5322.

153 Y. Ling, G. Wang, J. Reddy, C. Wang, J. Z. Zhang and Y. Li, *Angew. Chem., Int. Ed.*, 2012, **51**, 4074–4079.

154 S. Xiong, X. Lin, S. Liu, S. Weng, S. Jiang, Y. Jiao, Y. Xu and J. Cheng, *Vacuum*, 2020, **182**, 109692.

155 S. She, J. Yu, W. Tang, Y. Zhu, Y. Chen, J. Sunarso, W. Zhou and Z. Shao, *ACS Appl. Mater. Interfaces*, 2018, **10**, 11715–11721.

156 Y. Zhao, H. An, G. Dong, J. Feng, T. Wei, Y. Ren and J. Ma, *Chem. Eng. J.*, 2020, **388**, 124371.

157 W. Xie, F. Zhou, X. Bi, D. Chen, Z. Huang, Y. Li, S. Sun and J. Liu, *Chemosphere*, 2019, **221**, 563–572.

158 S. Zhao, D. Kang, Y. Liu, Y. Wen, X. Xie, H. Yi and X. Tang, *ACS Catal.*, 2020, **10**, 11739–11750.

159 N. Tian, X. Tian, Y. Nie, C. Yang, Z. Zhou and Y. Li, *Chem. Eng. J.*, 2019, **355**, 448–456.

160 F. Liu, W. Jin, Y. Li, L. Zheng, Y. Hu, X. Xu, Y. Xue, C. Tang, H. Liu and J. Zhang, *Appl. Surf. Sci.*, 2020, **529**, 147125.

161 K.-L. Yan, X. Shang, Z.-Z. Liu, B. Dong, S.-S. Lu, J.-Q. Chi, W.-K. Gao, Y.-M. Chai and C.-G. Liu, *Int. J. Hydrogen Energy*, 2017, **42**, 24150–24158.

162 W. Liu, J. Liu, P. Zhou, R. A. Dahlgren and X. Wang, *J. Colloid Interface Sci.*, 2022, **606**, 688–695.

163 X. Wei, X. Xie, Y. Wang and S. Yang, *J. Environ. Eng.*, 2020, **146**, 04020005.

164 J.-Y. Park, Y.-J. Lee, P. K. Khanna, K.-W. Jun, J. W. Bae and Y. H. Kim, *J. Mol. Catal. A: Chem.*, 2010, **323**, 84–90.

165 H.-J. Qiu, Y. Ito, W. Cong, Y. Tan, P. Liu, A. Hirata, T. Fujita, Z. Tang and M. Chen, *Angew. Chem., Int. Ed.*, 2015, **54**, 14031–14035.

166 Y. J. Sa, D.-J. Seo, J. Woo, J. T. Lim, J. Y. Cheon, S. Y. Yang, J. M. Lee, D. Kang, T. J. Shin, H. S. Shin, H. Y. Jeong, C. S. Kim, M. G. Kim, T.-Y. Kim and S. H. Joo, *J. Am. Chem. Soc.*, 2016, **138**, 15046–15056.

167 H. Wei, K. Huang, D. Wang, R. Zhang, B. Ge, J. Ma, B. Wen, S. Zhang, Q. Li, M. Lei, C. Zhang, J. Irawan, L.-M. Liu and H. Wu, *Nat. Commun.*, 2017, **8**, 1490.

168 L. Peng, X. Duan, Y. Shang, B. Gao and X. Xu, *Appl. Catal., B*, 2021, **287**, 119963.

169 Y. Lei, F. Yang, H. Xie, Y. Lei, X. Liu, Y. Si and H. Wang, *J. Mater. Chem. A*, 2020, **8**, 20629–20636.

170 X. Wang, J. Du, Q. Zhang, L. Gu, L. Cao and H.-P. Liang, *Carbon*, 2020, **157**, 614–621.

171 P. Su, M. Zhou, G. Ren, X. Lu, X. Du and G. Song, *J. Mater. Chem. A*, 2019, **7**, 24408–24419.

172 J. Wang, C. Liu, J. Qi, J. Li, X. Sun, J. Shen, W. Han and L. Wang, *Environ. Pollut.*, 2018, **243**, 1068–1077.

173 D. Du, W. Shi, L. Wang and J. Zhang, *Appl. Catal., B*, 2017, **200**, 484–492.

174 W. Lee and S.-J. Park, *Chem. Rev.*, 2014, **114**, 7487–7556.

175 P. Wang, X. Liu, W. Qiu, F. Wang, H. Jiang, M. Chen, W. Zhang and J. Ma, *Water Res.*, 2020, **182**, 116030.

176 C. Gao, F. Lyu and Y. Yin, *Chem. Rev.*, 2021, **121**, 834–881.

177 S. Valange, R. Palacio, A. Charmot, J. Barrault, A. Louati and Z. Gabelica, *J. Mol. Catal. A: Chem.*, 2009, **305**, 24–33.

178 A. Li, W. Zhu, C. Li, T. Wang and J. Gong, *Chem. Soc. Rev.*, 2019, **48**, 1874–1907.

179 W. Wang, M. Ding, L. Ma, X. Yang, J. Li, N. Tsubaki, G. Yang, T. Wang and X. Li, *Fuel*, 2016, **164**, 347–351.